

Journal Pre-proof

Understanding the sulfate attack of Portland cement-based materials exposed to applied electric fields: Mineralogical alteration and migration behavior of ionic species

Chen Li, Zhengwu Jiang, Rupert J. Myers, Qing Chen, Mengxue Wu, Jiaqi Li, Paulo J.M. Monteiro



PII: S0958-9465(20)30122-0

DOI: <https://doi.org/10.1016/j.cemconcomp.2020.103630>

Reference: CECO 103630

To appear in: *Cement and Concrete Composites*

Received Date: 14 September 2019

Revised Date: 11 March 2020

Accepted Date: 9 April 2020

Please cite this article as: C. Li, Z. Jiang, R.J. Myers, Q. Chen, M. Wu, J. Li, P.J.M. Monteiro, Understanding the sulfate attack of Portland cement-based materials exposed to applied electric fields: Mineralogical alteration and migration behavior of ionic species, *Cement and Concrete Composites* (2020), doi: <https://doi.org/10.1016/j.cemconcomp.2020.103630>.

This is a PDF file of an article that has undergone enhancements after acceptance, such as the addition of a cover page and metadata, and formatting for readability, but it is not yet the definitive version of record. This version will undergo additional copyediting, typesetting and review before it is published in its final form, but we are providing this version to give early visibility of the article. Please note that, during the production process, errors may be discovered which could affect the content, and all legal disclaimers that apply to the journal pertain.

© 2020 Published by Elsevier Ltd.

1 **Understanding the sulfate attack of Portland cement-based materials exposed to applied**
2 **electric fields: Mineralogical alteration and migration behavior of ionic species**

3

4 Chen Li ^{a,b}, Zhengwu Jiang ^{a,*}, Rupert J. Myers ^{c,d}, Qing Chen ^a, Mengxue Wu ^{a,e}, Jiaqi Li ^b, Paulo J. M. Monteiro ^{b,f}

5

6 ^a *Key Laboratory of Advanced Civil Engineering Materials of Ministry of Education, Tongji University, 4800
7 Cao'an Road, Shanghai, 201804, China*

8 ^b *Department of Civil and Environmental Engineering, University of California, Berkeley, California, 94720,
9 United States*

10 ^c *School of Engineering, University of Edinburgh, Edinburgh, EH9 3FB, United Kingdom*

11 ^d *Current address: Department of Civil and Environmental Engineering, Imperial College London, London, SW7
12 2AZ, United Kingdom*

13 ^e *Administration for Market Regulation of Chengdu, Sichuan, 610044, China*

14 ^f *Material Science Division, Lawrence Berkeley National Laboratory, Berkeley, California, United States*

15

* Corresponding author

E-mail address: jzhw@tongji.edu.cn (Z. Jiang).

16 **Abstract**

17

18 The magnesium and sodium sulfate attacks on Portland cement paste in the presence of applied electric fields were
19 studied, and the mineralogical alterations were investigated by both experiments and thermodynamic modeling.
20 When an electric current flows out of the cement paste, the electric migration of ions induced sulfate ingress and
21 decalcification. Compared with the specimen exposed to Na_2SO_4 , that exposed to MgSO_4 for 28 d proceeded to a
22 later degradation stage, which is characterized by the decomposition of ettringite, portlandite, and AFm phases, and
23 the formation of CaSO_4 . Thermodynamic modeling indicates a neutralization process induced by the electric
24 migration of OH^- , which is potentially responsible for the decomposition of ettringite. When an electric current
25 flows into the cement paste, the Mg^{2+} and Na^+ showed different migration behavior. Mg^{2+} was incorporated to form
26 brucite and M-S-H-like products in a shallow area ($\sim 100 \mu\text{m}$) on the surface of the specimen, whilst a part of the
27 Na^+ could be bonded to form Na-rich silica gel with the other part penetrating through the specimen. By coupling
28 the pore solution chemistry obtained from thermodynamic modeling with the Nernst-Planck equation, the migration
29 behaviors of the ionic species (SO_4^{2-} , Mg^{2+} , and Na^+) were analyzed.

30

31 **Keywords**

32

33 Sulfate attack; Mineralogical alteration; Thermodynamic modeling; Nernst-Planck equation; Applied electric field

34

35 **1 Introduction**

36

37 Cement-based materials are porous and consist of multiple phases. The hydration products (solid phase) form the

38 skeleton of the pore structures, and the pore solution (aqueous phase) and air (gaseous phase) fill inside the pores.

39 In a fully hydrated cement paste, the hydration products are approximately at equilibrium with the pore solution.

40 However, this state will be affected by the ionic exchange between the pore solution and the external environment.

41 Such a process usually induces mineralogical alterations and is described as a chemical attack. The attack is

42 affected by the type, rate, and direction of the ion exchange, as well as the chemical reactions that occur.

43

44 The ingress of external sulfate will cause sulfate attack, which is one of the most widely recognized and

45 well-studied chemical attacks. In Portland cement systems, sulfate attacks are usually characterized by the

46 formation of ettringite, and by the expansion, cracking, and strength loss thereafter [1-3]. Recent theories relate the

47 expansion to the crystallization pressure caused by the formation of ettringite from oversaturated solution in small

48 pores [4-6]. The crystals growing in confined pores, e.g., in the C-S-H gel, generate crystallization pressure and

49 thus expansive stress [7,8], whilst those growing in unrestrained pore spaces do not. Gypsum usually forms at the

50 late stage of sulfate attack. There was once a debate on whether the formation of gypsum is a cause [9-11] or an

51 effect [12,13] of the expansion and cracking. Recent studies proposed that the presence of gypsum induces a high

52 supersaturation with respect to ettringite, and thus a high crystallization pressure and more expansion [2,14,15].

53

54 The type of cation that coincides with sulfate greatly influences the degradation process. When the cation is Mg²⁺,

55 surface erosion occurs in addition to expansion [15-17]. This phenomenon is induced by the formation of brucite

56 and magnesium silicate hydrate (M-S-H) [2,16], and is the most important characteristic to distinguish magnesium

57 sulfate attack from sodium sulfate attack. It was also reported that the co-existence of Na⁺, K⁺, and Ca²⁺ can reduce

58 surface erosion and expansion in the MgSO₄ attack [2,16]. When the sulfate is provided by an acidic environment,

59 neutralization can take place in the pore solution, and the Ca²⁺ can diffuse towards the external environment due to

60 the concentration gradient. Under this circumstance, calcium leaching or decalcification will also occur together
61 with the sulfate attack [18-20].

62

63 In most cases, the ionic exchange between cement-based materials and the external environment is driven by the
64 concentration gradient, and this process is known as diffusion. In certain field conditions, the exposed surface of a
65 structure is subjected to strong evaporation conditions. The moisture gradient between the external environment
66 and cement-based materials induces capillary suction, and the ionic species will be transported by advection [21].

67 Under an applied electric field, the ionic species in the pore solution can also migrate, which is known as electric
68 migration [22-24]. The transportation of ionic species—their diffusion, advection, and electric migration in
69 cement-based materials is described by the Nernst-Planck equation [22-25]. During the ionic transportation,
70 chemical reactions can take place. For example, SO_4^{2-} can react with monosulfate to form ettringite [1,20,26]. This
71 reaction impacts not only the mass transport of SO_4^{2-} but also the strength of Ca^{2+} and AlO_2^- by disturbing the
72 equilibrium between the hydration products and the pore solution. In this respect, the concurrent chemical reactions
73 and ionic transportation both play significant roles in the ingress of sulfate.

74

75 In some cases, cement-based materials are directly exposed to applied electric fields, e.g., the DC stray current that
76 is present in underground metro tunnels [27-29]. Electric migration can accelerate the ingress of aggressive ions
77 from the external environment and remove the calcium and alkali metals from the pore solution [30,31]. Electric
78 fields are also applied in some modern concrete techniques, e.g., chloride extraction, realkalinization, cathodic
79 protection, and electrochemical deposit [32-35]. In these techniques, certain types of ions are designed to migrate,
80 but the migrations of other ions have to be considered because they may induce side effects [36]. Electric migration
81 is also a useful tool for laboratory acceleration tests, e.g., the chloride ion penetration tests (ASTM C1202), calcium

82 leaching acceleration tests [37,38], etc. Recent studies proposed that electric migration tests can be potentially used
83 in the acceleration of sulfate attacks [39-41]. However, a deeper understanding of the mineralogical alterations and
84 the degradation mechanism under such circumstances will be needed to evaluate the validity of this technique.

85

86 In a conventional sulfate attack caused by diffusion, both the cations and anions in the external solution diffuse into
87 the cement-based materials, while the ions in the pore solution, e.g. Ca^{2+} , OH^- , and alkali metal ions diffuse
88 outward. In contrast, under applied electric fields, the cations and anions migrate in different directions, and thus
89 the degradation behavior and mechanism may differ from the diffusion-induced sulfate attacks. This paper studies
90 the MgSO_4 and Na_2SO_4 attacks on Portland cement paste in the presence of applied electric fields. The chemical
91 and mineralogical alterations during the degradation process were analyzed by scanning electron microscopy
92 (SEM), energy dispersive X-ray spectrometry (EDS), X-ray diffractometry (XRD), and thermogravimetric analysis
93 (TGA). The results suggest different degradation behaviors between the areas near the cathode and anode, and
94 between the specimens exposed to different sulfate sources. To better understand the degradation mechanism, an
95 approach was proposed to simplify the electric migration processes, and changes of the phase assemblages during
96 the simplified electric migration processes were then calculated by thermodynamic modeling. By combining the
97 pore solution chemistry obtained in the thermodynamic modeling with the Nernst-Planck equation, the migration
98 behaviors of various ionic species were analyzed to explain the different degradation behaviors observed
99 experimentally.

100

101 **2 Experimental**

102 *2.1 Cement paste specimens*

103

104 Cement paste specimens were prepared using Portland cement and deionized water at a water-to-cement ratio of 0.5.
 105 The chemical composition of the Portland cement was tested by X-ray fluorescence spectrometry (XRF), and the
 106 mineralogical composition was measured by XRD and analyzed by Rietveld refinement, as shown in Table 1. The
 107 specimens were cast into cylindrical molds that were 100 mm in diameter and 50 mm in height, cured at 20 °C ±
 108 1 °C, RH > 95% and unmolded after 24 h. The top of the cylinders, which was not in contact with the molds, was
 109 polished by P240 (58 µm) sandpaper to make it flat and smooth. The specimens were then cured in saturated
 110 limewater at 20 °C ± 1 °C until 28 d.

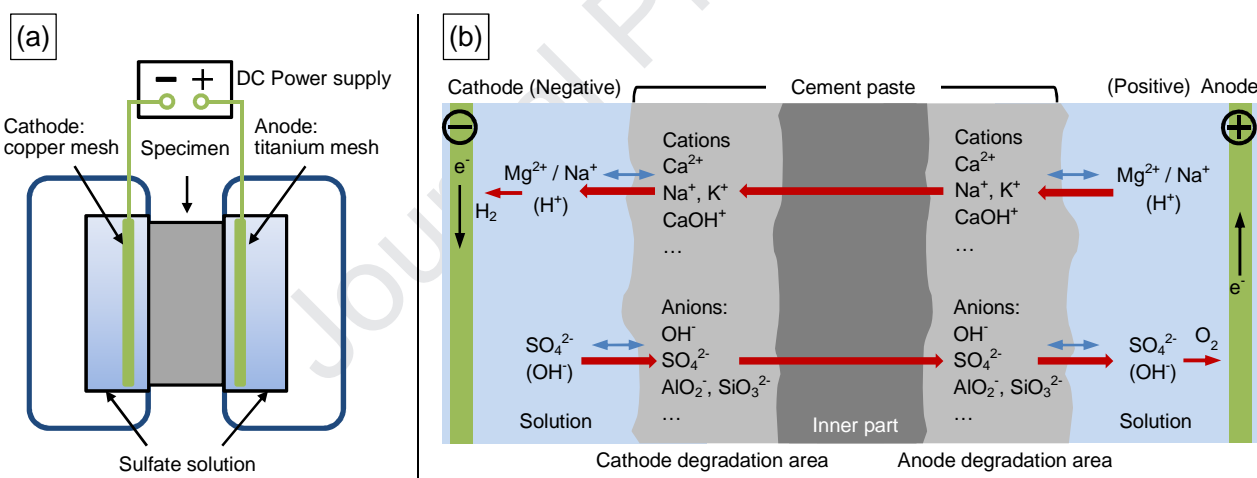
111
 112 **Table 1** Chemical and mineralogical compositions of the Portland cement (wt. %).

Chemical composition		Mineralogical composition	
Na ₂ O	0.04	C ₃ S	58.32
MgO	0.76	C ₂ S	11.64
Al ₂ O ₃	4.55	C ₃ A	3.96
SiO ₂	20.8	C ₄ AF	8.03
P ₂ O ₅	0.11	Calcite	4.58
SO ₃	2.92	Anhydrite	0.76
K ₂ O	0.74	Bassanite	3.67
CaO	64.8	Gypsum	0.01
TiO ₂	0.23	Lime	0.35
Cr ₂ O ₃	0.02	Portlandite	0.58
MnO	0.11	CF ₂	1.53
Fe ₂ O ₃	3.27	Goergeyite	3.30
CuO	0.02	Perovskite	1.79
ZnO	0.05	Periclase	0.85
SrO	0.03	Dolomite	0.13
LOI	2.58	Quartz	0.21

113
 114 2.2 *Electric field application*
 115
 116 The electric field was applied by electrolytic cells similar to those for the chloride ion penetration tests described in
 117 ASTM C1202 (Fig. 1a). The anode was a titanium mesh, and the cathode was a copper mesh. A constant electric

118 current of 30.0 mA (equal to $\sim 4.71 \text{ A/m}^2$) was maintained by a DC power supply. The cells on both sides were
 119 filled with the same sulfate solution, either 0.5 mol/L MgSO_4 or 0.5 mol/L Na_2SO_4 . This concentration is slightly
 120 higher than the one used in the sulfate expansion tests in ASTM C1012 (5% Na_2SO_4 , $\sim 0.35 \text{ mol/L}$). The solutions
 121 were prepared using deionized water and sodium sulfate anhydrous (Sinopharm, purity > 99.0%) or magnesium
 122 sulfate heptahydrate (Sinopharm, purity > 99.0%), and were refreshed every three days. An estimation based on
 123 charge conservation shows that the concentration of the sulfate solutions can remain higher than $\sim 0.34 \text{ mol/L}$
 124 during the experiment (see Supplementary Data). For either MgSO_4 or Na_2SO_4 , three sets of electrolytic cells were
 125 set up. The specimens were taken out after exposure to the applied electric fields for 7, 14, and 28 days. The
 126 deposits formed on the electrodes were cleaned every six days.

127



128

129 **Fig. 1.** Test setup to apply electric fields: (a) overview of the test setup and (b) schematic of ionic motion where
 130 thickness and velocity are not to scale. The ionic motion is driven by electric migration (red arrows) and diffusion
 131 (blue arrows).

132

133 Figure 1b illustrates the motion of ionic species in the test setup. The anode is connected to the positive output of
 134 the power supply and has a higher electric potential compared with the cathode. The cations in the anodic solution
 135 (Mg^{2+} or Na^+) migrate towards the cement paste and enter the specimen from the surface near the anode.
 136 Meanwhile, the cations in the pore solution (Ca^{2+} , Na^+ , K^+ , etc.) migrate towards the cathode and leave the

137 specimen from the nearby surface. The anions migrate in the opposite direction. Diffusion also occurs in addition to
138 electric migration. The ionic species in the external solution (SO_4^{2-} and $\text{Na}^+/\text{Mg}^{2+}$) diffuse towards the specimen on
139 both sides, and the ions in the pore solution also diffuse towards the external solutions.

140

141 Similar test setups are also used in [39-41] for accelerating sulfate attacks in the laboratory. The current density was
142 not reported in those literatures, and the estimated values were between one and several A/m^2 based on the voltage
143 and size of the specimen (assuming the resistivity of water-saturated cement mortar is around $10 \text{ k}\Omega\cdot\text{cm}$). For
144 studying the effects of DC stray current on reinforcement corrosion and concrete degradation, the current densities
145 of 1 and 10 A/m^2 were chosen in [27,42]. The current density used in this paper ($\sim 4.71 \text{ A/m}^2$) is comparable to
146 these reported values.

147

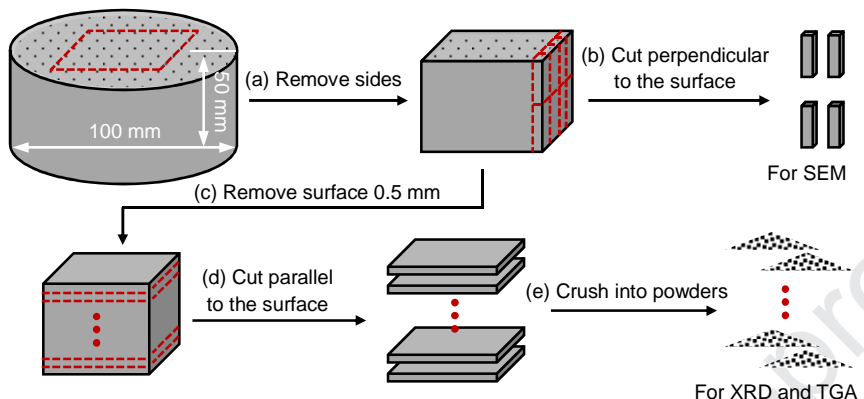
148 *2.3 Test method*

149

150 After the exposures to the applied electric fields for certain durations, the specimens were removed from the test
151 setups and cut into pieces according to the procedures in Fig. 2. Small patches that contain all the depth from the
152 exposure surface (0 mm) to ~ 25 mm were prepared for SEM. A face perpendicular to the exposure surface was
153 used for observation. These samples were impregnated with epoxy resin, polished on SiC discs and diamond
154 suspension-sprayed discs (Buehler), carbon-coated, and observed using a Quanta 200 FEG microscope in the
155 backscattered electron mode. The hydration products on the surface of the specimens usually showed clear features
156 (brightness and morphology), and the chemical composition of such well-resolved hydration products was analyzed
157 based on at least five EDS measurements. EDS point analyses were also conducted randomly in the well hydrated
158 areas (where the hydration products mingle and cannot be identified easily) to reflect the chemical composition of

159 the hydration products in such areas. The average chemical composition in several $50\text{ }\mu\text{m} \times 50\text{ }\mu\text{m}$ areas was
 160 measured to represent the distribution of elements along the depth from the exposure surface. The microstructure
 161 were analyzed by observing a 5-mm-wide area parallel to the surface.

162



163

164 **Fig. 2.** Preparation of samples: (a) the sides of a cylindrical specimen that were not well exposed to sulfate
 165 solutions were cut off, (b) small patches that were perpendicular to the exposure surface was cut for SEM,
 166 (c) the surface part (0.5 mm) of the remainder was removed, (d) the specimen was cut parallel to the exposure surface into
 167 5-mm thick slices, and (e) the slices were crushed into powders (particle size $<75\text{ }\mu\text{m}$) for XRD and TGA.

168

169 The powder samples for XRD and TGA were soaked in ethanol for 5 days to stop the hydration and then dried at
 170 $40\text{ }^\circ\text{C}$ for 24 h. XRD was conducted on a D/max2550VB3+/PC diffractometer equipped with Cu K_α radiation and
 171 a graphite monochromator. The X-ray generator was operated at 40 kV and 250 mA, the scanning range was $2\theta =$
 172 $5\text{--}75^\circ$, and the step size and counting time were 0.02° and 2 s, respectively. TGA was conducted on a NETZSCH
 173 STA 449C simultaneous thermal analyzer. The samples were heated under N_2 atmosphere from $40\text{ }^\circ\text{C}$ to $950\text{ }^\circ\text{C}$
 174 with a heating rate of $10\text{ }^\circ\text{C}/\text{min}$. The data were expressed as differential thermogravimetry, and the peaks were
 175 assigned according to [43]. Note that the specimens for XRD and TGA did not include the surface part ($\sim 0.5\text{ mm}$),
 176 because this part was quite different in composition from the other parts according to SEM but its material amount
 177 was not sufficient for these tests.

178

179 2.4 Rietveld refinement

180

181 Corundum (α -Al₂O₃, Aladdin, purity > 99.99%) was used as an internal standard. It was mixed with the dried
 182 powder samples at a mass ratio of 10 to 90. The Rietveld refinement was conducted using TOPAS Academic V5.
 183 The crystallographic models were obtained from the Inorganic Crystal Structure Database (ICSD), see
 184 Supplementary Data. The optimized parameters included the background coefficient, zero-shift error, crystal size L,
 185 and lattice parameters (restrained within $\pm 0.5\%$). The peak shape was described by the fundamental parameter (FP)
 186 approach employed in TOPAS. The March-Dollase ellipsoidal preferred orientation correction algorithm [44] was
 187 employed for Alite-M3 (606) [45], portlandite (001) [46], and calcite (104) [45]. Two peaks using fundamental
 188 parameters were added near $2\theta = 29.3^\circ$ and 50.0° to simulate the broad peaks produced by C-S-H [47,48]; and the
 189 scale factor, crystal size L, and position of the peaks were refined.

190

191 2.5 Simplifications in the thermodynamic modeling of the degradation process

192

193 In order to gain insight into the chemical and mineralogical aspects of the degradation process and study the
 194 degradation mechanism, a simplified approach was proposed to represent the main processes of electric migration.
 195 Based on this simplified approach, the phase assemblage during degradation was further studied by thermodynamic
 196 modeling. Here, electric migration is assumed to be the only driving force for the ionic motion and described by the
 197 Nernst-Planck equation [22-25] as

$$J_{i,e} = -D_i^a \cdot \frac{z_i F}{RT} C_i \frac{\partial \Psi}{\partial x} \quad (1)$$

198 where $J_{i,e}$ ($\text{mol} \cdot \text{m}^{-2} \cdot \text{s}^{-1}$) is the bulk flux of ionic species i at location x ; D_i^a ($\text{m}^2 \cdot \text{s}^{-1}$) is the apparent diffusion
 199 coefficient; z_i is the charge number; C_i ($\text{mol} \cdot \text{m}^{-3}$) is the ionic strength; $F = 9.648 \times 10^{-4} \text{ C} \cdot \text{mol}^{-1}$ is the Faraday

200 constant; $R = 8.314 \text{ J}\cdot\text{mol}^{-1}\cdot\text{K}^{-1}$ is the gas constant; T (K) is the absolute temperature; and Ψ (V) is the electric
 201 potential. The apparent diffusion coefficient usually has a positive relationship with the corresponding diffusion
 202 coefficient in free water (D_i^0 in $\text{m}^2\cdot\text{s}^{-1}$), and this relationship is impacted by the pore structure characterized by
 203 porosity (φ) and tortuosity (τ) as [23]

$$D_i^a = \frac{\varphi}{\tau^2} D_i^0 \quad (2)$$

204
 205 When an electric field is applied, the migration rate of an ion depends on its charge number, concentration, and
 206 diffusion coefficient in free water. The diffusion coefficient in free water can be obtained from the chemistry
 207 handbook [49], and the concentration of ions in the cement paste before exposure to electric fields can be calculated
 208 by thermodynamic modeling (see Supplementary Data), as shown in Table 2.

209
 210 **Table 2** Concentration of ions in the pore solution before degradation and diffusion coefficient in free water (D_i^0).

	Concentration mol/L	Diffusion coefficient $10^9 \text{ m}^2/\text{s}$	Direction
OH^-	2.05×10^{-1}	5.273	
SO_4^{2-}	6.79×10^{-4}	1.065	
AlO_2^-	4.25×10^{-5}	n.a. ¹	
SiO_3^{2-}	9.94×10^{-6}	n.a. ¹	Cathode → inner part → anode → anodic solution
CO_3^{2-}	4.66×10^{-5}	n.a. ¹	
HCO_3^-	2.27×10^{-8}	1.185	
Ca^{2+}	1.01×10^{-3}	0.792	
Ca(OH)^+	9.09×10^{-4}	n.a. ¹	
Mg^{2+}	1.11×10^{-10}	0.706	Anode → inner part → cathode → cathodic solution
Na^+	2.34×10^{-3}	1.334	
K^+	2.01×10^{-1}	1.957	

211 ¹ Not available in [49].
 212

213 As illustrated in Fig. 1b, it is assumed that each specimen contains two degradation areas that are located on the
 214 exposure surfaces and are affected by the chemical attack, while the inner part between these two degradation areas
 215 is not affected. At the beginning of degradation, the pore solution chemistry and pore structure are similar in all

216 parts across the cement paste, and the electric gradient is uniform. In the pore solution, ionic species i at different
 217 positions will migrate at the same rate according to Eq. 1. In the degradation area near the cathode, the cations are
 218 released into the cathodic solution due to electric migration, but they are also supplemented by those migrating
 219 from the inner part of the specimen at the same rate. The anions in the pore solution migrate towards the inner part
 220 and are replaced by those from the cathodic solution. However, the migration rate of the anions from the cathodic
 221 solution into the cement paste is difficult to determine, because the electric gradient and pore structure are different
 222 between the surface of a specimen and its interior. Here, it is assumed that the replacement of the anions in the
 223 degradation area near the cathode maintains the charge balance. Similarly, the main process in the degradation area
 224 near the anode is the replacement of cations in the pore solution by those from the anodic solution in a
 225 charge-balanced manner. These processes are similar to those reported in numerical simulation studies of the rapid
 226 chloride migration test [23,50]. Here, they are defined as the “basic state” of electric migration, which is a transient
 227 state when the concentration of the ions in the pore solution is similar to that before degradation initiates. The
 228 duration of the basic state depends on whether the concentration of the ionic species in the pore solution remains
 229 stable during the ionic exchange and the relevant chemical reactions.

230

231 In the pore solution, the concentration of OH^- is higher than the other anions by three orders of magnitude (Table 2),
 232 and the main anion in the cathodic solution (a neutral Na_2SO_4 or MgSO_4 solution) is SO_4^{2-} . According to Eq. 1,
 233 these two ionic species migrate much faster than the others in the pore solution and the cathodic solution,
 234 respectively. Moreover, the decomposition of portlandite can somewhat help maintain the ionic strength of OH^- in
 235 the pore solution, which is known as the buffering effect [51]. Therefore, the electric migration process near the
 236 cathode is simplified to the replacement of each two moles of OH^- by one mole of SO_4^{2-} .

237

238 In the area near the anode, K^+ and Na^+ are the most easily migrated ionic species. However, they will be removed
239 quickly due to their low contents in the hydrated cement paste [23,50], indicating that this state is short-lived.
240 Afterward, Ca^{2+} will be the main ionic species to migrate. ($CaOH^+$ will also migrate, but its effect on the
241 mineralogical alteration is similar to that of Ca^{2+} .) Its ionic strength can be maintained by the buffering effect,
242 suggesting a possibly longer duration. Therefore, the electric migration process in this state is simplified by
243 replacing each mole of Ca^{2+} with one mole of Mg^{2+} or two moles of Na^+ , based on a hydrated system without K
244 and Na.

245

246 *2.6 Thermodynamic modeling*

247

248 Thermodynamic modeling was performed using the geochemical code GEMS 3.3 [52] with the Nagra/PSI database
249 [53] and CEMDATA 18 database (version 18.01) [54]. The CSHQ model was selected. The solid solutions of AFt
250 and AFm were not considered. Siliceous hydrogarnet ($C_3AS_{0.8}H_{4.4}$) and thaumasite usually form at slow kinetics at
251 the ambient temperature [55,56]. The presence of electric fields does not significantly impact the slow formation
252 kinetics of thaumasite [57], but it remains unknown whether the formation kinetics of $C_3AS_{0.8}H_{4.4}$ will be
253 influenced. These products were both suppressed in the modeling.

254

255 First, the phase assemblage before sulfate ingress was calculated. The following hydration degrees were assumed
256 based on the XRD results at an age of 28 d: 95% for C_3S , 65% for C_2S , 100% for C_3A , and 70% for C_4AF . The
257 Na_2O and K_2O in the cement were assumed to dissolve completely, while the MgO was assumed to dissolve by
258 90%. Calcite was set to react freely [58].

259

260 The hydration phase assemblage during the electric migration process was then calculated by changing the input
 261 recipe according to the simplified approach (see Supplementary Data). In order to further analyze the migration rate
 262 of the ionic species in the pore solution during degradation, the theoretical flux of OH⁻ in the pore solution at the
 263 beginning of degradation was considered as a reference. Provided that the pore structure in Eq. 2 does not change
 264 significantly during degradation, the relative flux (R) of a type of ionic species i is hereby defined as

$$R = \frac{J_{i,e}}{J_{OH,e}} = \frac{D_i^0 z_i C_i}{D_{OH}^0 z_{OH} C_{OH}^0} \quad (3)$$

265
 266 At a given time during the electric migration process, an ion with higher relative flux migrates faster, provided that
 267 the flux is uniform in the cross-section. In addition to their migration, the concentration of ions in the pore solution
 268 may also be affected by the phase changes induced by electric migration, and the manner of ionic migration may
 269 thus deviate from the description of the simplified processes. This effect can also be represented by the changes in
 270 the relative flux.

271

272 **3 Results**

273 *3.1 Test results of MgSO₄ exposure*

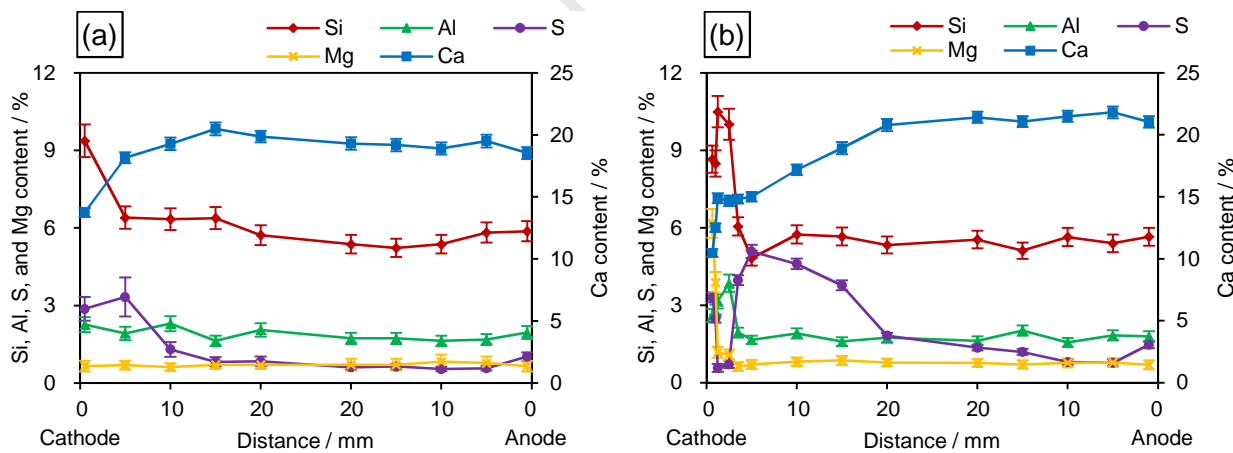
274 3.1.1 Chemical composition and microstructural alterations

275

276 Near the cathode, an exposure to MgSO₄ in the presence of applied electric fields increased the S content of the
 277 cement paste (Fig. 3, see from the left). The S content near the surface (e.g., 0.1–10 mm) increased with the
 278 exposure time and became higher than that of the inside part (e.g., 20 mm). In addition, the Ca content near the
 279 surface decreased whilst the Si and Al contents increased. An enrichment of Mg was observed at a depth of 0.1–
 280 0.25 mm after an exposure time of 28 d (Fig. 3b). In addition to the chemical composition alteration, the surface

area near the cathode (0–3 mm) showed a layered microstructure (Fig. 4a). In the outermost layer (0–300 µm, area I), a large amount of CaSO₄ formed on the surface of the specimen, and the hydration products decalcified to form silica-alumina gel (e.g., Spot A of Fig. 4b). Deeper inside the cement paste (300–1000 µm, area II), the hydration products were affected by both decalcification and magnesium ingress. The silica-alumina gel showed a high Mg content (Spot A of Fig. 4c), which agrees with the Mg enrichment in this area (Fig. 3b). CaSO₄ was also present in this area (Spot B of Fig. 4c). About 1–3 mm from the surface (area III), the hydration products were not impacted by the ingress of either magnesium or sulfate. The cement paste was porous (Fig. 4d). The Ca/Si ratio of the hydration products in this area was typically smaller than 1.5, which coincides with the chemical composition shown in Fig. 3b. From 3 mm inside (area IV), the cement paste started to show continuous alterations without layered structures.

291



292

Fig. 3. Chemical composition at different distances from the surface (cathode on the left and anode on the right) after exposure to MgSO₄ for (a) 7 d and (b) 28 d. Each data point represents the average over a 50 µm × 50 µm area measured by EDS. Error bars indicate the standard error in ZAF matrix correction schemes. The sampling points nearest to the surfaces are 0.1 mm from the surface.

297

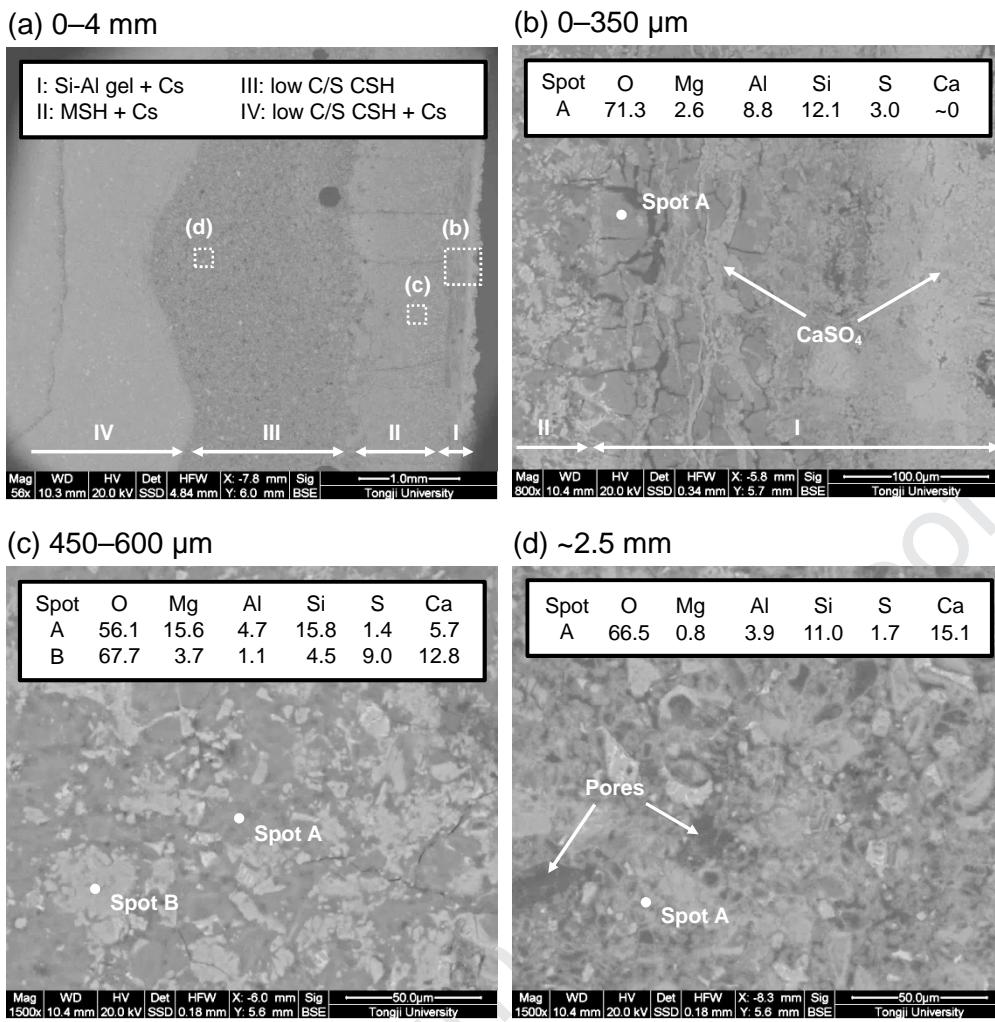


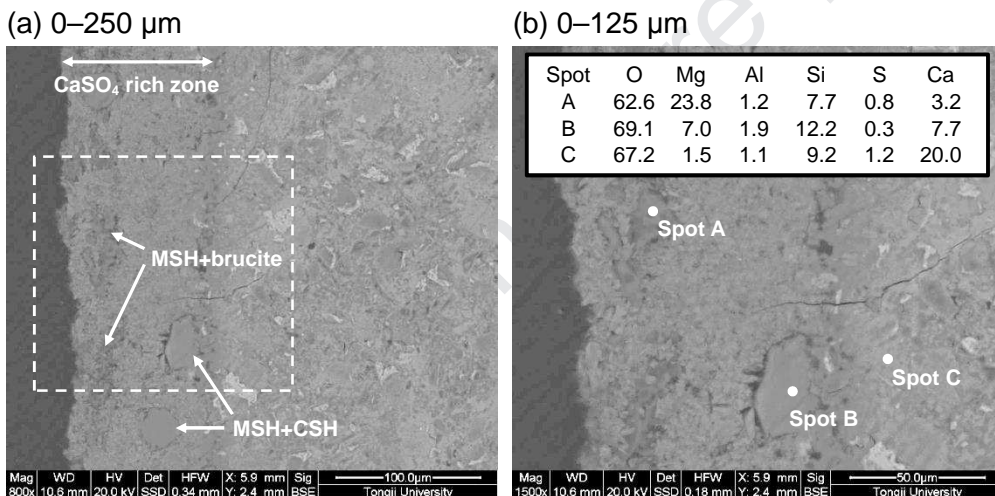
Fig. 4. Microstructure of the surface area (0–4 mm) near the cathode after 28 d exposure to MgSO₄: (a) an overview, and (b) to (d) enlargements of the squared areas. Surface on the right.

302

303 The cement paste near the anode did not show significant alterations on both chemical composition (Fig. 3, see
304 from the right) and microstructure (Fig. 5). A very small increase of the S content was observed in the surface area
305 (0.1 mm from the surface). Considering the direction of electric migration (Fig. 1b), the increased S content is
306 mainly induced by diffusion [39,40]. The Mg²⁺ in the anodic solution should theoretically move towards the cement
307 paste due to electric migration (Fig. 1b). However, the ingress of Mg²⁺ was constrained within a depth of ~100 µm
308 according to SEM. (Fig. 5). This 100-µm-zone was rich in CaSO₄, and two types of Mg-containing products with
309 different brightness and Mg/Si ratio were found. Closer to the surface, some Mg-containing products in clusters
310 were embedded in the CaSO₄. These products were darker than the hydration products nearby. The Mg/Si ratio was

higher than 3 (Spot A), which potentially indicates a mixture of M-S-H and brucite on the microscale. Similar products were also reported to form on the surface of the cement mortar after the magnesium sulfate attack in the absence of applied electric fields [15,16]. Farther from the exposure surface, there were some larger particles (Spot B). Compared with the Mg-containing products in clusters (Spot A), the Mg/Si ratio of these particles was much lower, and the Ca content was higher. This chemical composition led to a slightly higher brightness and may represent a mixture of M-S-H and C-S-H, or an M-C-S-H [59]. Next to the CaSO_4 -rich zone, the Ca/Si ratio of the hydration products was typically higher than 1.5, and no magnesium-containing products were observed, which is also verified in Fig. 3b.

319



320

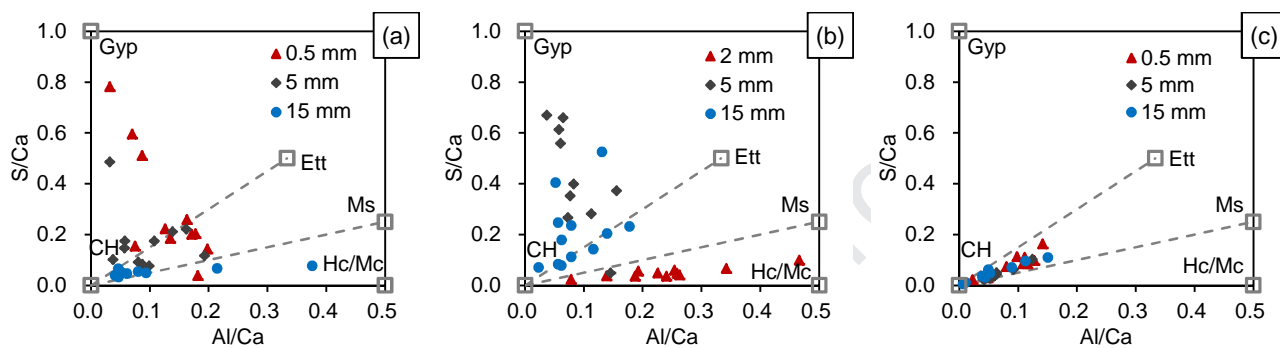
Fig. 5. Microstructure of the surface area (0–250 μm) near the anode after 28 d exposure to MgSO_4 : (a) an overview and (b) enlargement of the squared area. Surface on the left.

323

EDS spot analyses were conducted randomly at certain depths, and the S/Ca is plotted against the Al/Ca in Fig. 6. After an exposure time of 7 d (Fig. 6a), the chemical composition of the hydration products indicates the presence of CaSO_4 and ettringite at the depths of 0.5 mm and 5 mm from the cathode. A small amount of ettringite may exist at the depth of 15 mm. After an exposure time of 28 d (Fig. 6b), the hydration products at 2 mm from the cathode (area III, Fig. 4a) showed very small S/Ca and relatively high Al/Ca to the other groups, coinciding with the

329 decalcification observed in Spot A, Fig. 4d. CaSO_4 was suggested to be the dominant sulfate-bearing phase at 5 mm
 330 from the cathode (area IV, Fig. 4a), and a large amount of CaSO_4 with ettringite in a minor proportion may be
 331 present at 15 mm from the cathode. In the areas that are 0.5 mm, 5 mm, and 15 mm from the anode (Fig. 6c), the
 332 hydration products may contain a mixture of ettringite, monosulfate, C-S-H, and portlandite.

333



334
 335 **Fig. 6.** Atom ratio plots of S/Ca against Al/Ca at different depths from the surface after exposures to MgSO_4 : (a)
 336 and (b) the cathode areas exposed to MgSO_4 for 7 d and 28 d, respectively; (c) the anode areas exposed to MgSO_4
 337 for 28 d. CH = Portlandite (and C-S-H at a similar position), Ett = Ettringite, Ms = Monosulfate, Hc/Mc =
 338 Hemicarbonate or monocarbonate , Gyp = CaSO_4 .

339

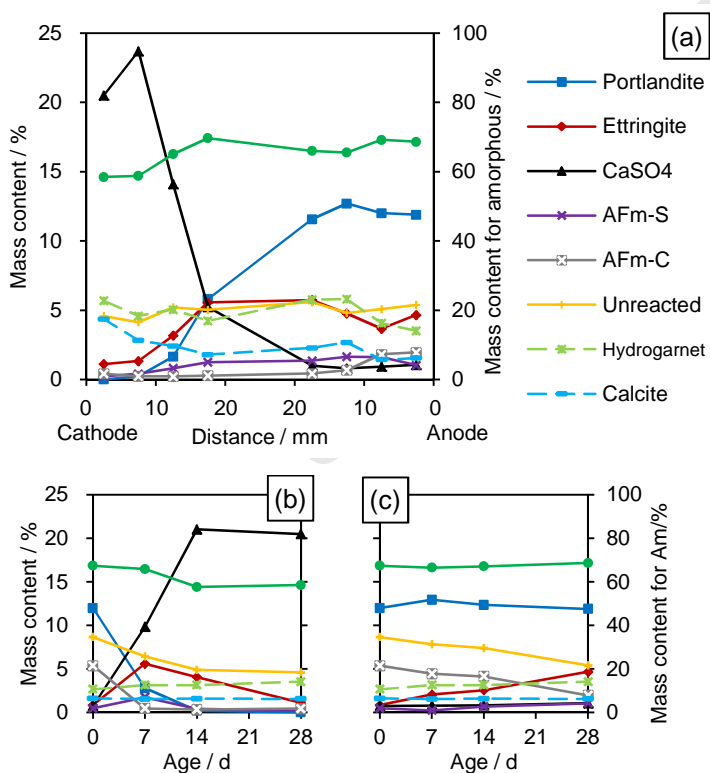
340 3.1.2 Mineralogical alteration

341

342 In the cement paste near the cathode, the formation of sulfate-bearing products and decomposition of portlandite
 343 were observed. After 28 d exposure to MgSO_4 , the cement paste nearest to the surface (0.5–5 mm) contained almost
 344 no portlandite or ettringite, but a large amount of CaSO_4 (Fig. 7a, see from the left). The CaSO_4 content was
 345 slightly higher at 5–10 mm than that of the surface part, and started to decrease beyond this depth. Portlandite and
 346 ettringite were detected beyond the depth of 10 mm, and their contents increased with the depth. In addition to the
 347 decomposition of portlandite, the amorphous content in the cement paste near the cathode also showed a reduction.
 348 Fig. 7b shows that the formation of ettringite and CaSO_4 started even before 7 d, during which the decomposition
 349 of portlandite had been significant. Between 7–14 d, the formation of CaSO_4 continued while ettringite started to

350 decompose. Almost no portlandite could be detected by 14 d, and the CaSO_4 content remained almost constant
 351 afterward. Monocarbonate and hemicarbonate were observed due to the hydration of limestone [56,58]. These
 352 products had formed before the exposure to MgSO_4 but started to decompose after the exposure. Almost no AFm
 353 phases remained near the cathode after an exposure time of 7 d (Fig. 7b). Magnesium-bearing products were not
 354 observed in XRD, which agrees with the small penetration depth of Mg^{2+} shown in Fig. 3 and Fig. 4. However,
 355 brucite was observed to form in the cathodic solution, which mingles with other products and forms a thick layer of
 356 deposits on the electrode. The deposits collected on the 28th exposure day and tested by XRD suggested a mixture
 357 of 40.2% brucite, 41.1% gypsum, 14.5% portlandite, 3.3% anhydrite, and 0.8% calcite.

358



359

360 **Fig. 7.** Mineralogical composition of the specimen exposed to MgSO_4 obtained by XRD and Rietveld refinement:
 361 (a) all the depths after 28 d exposure time; (b) and (c) phase alteration of the 0.5–5 mm area near the cathode and
 362 anode, respectively, after different exposure time. CaSO_4 = anhydrite + bassanite + gypsum, AFm-S = monosulfate,
 363 AFm-C = monocarbonate + hemicarbonate, hydrogarnet = katoite + hydrogrossular.

365

366 In the anode area, the ettringite content in the 0.5–5 mm area increased slowly with the exposure time, and the

367 contents of monocarbonate and hemicarbonate decreased (Fig. 7c). After 28 d, the ettringite content in this area was
368 slightly higher than that of the 5–10 mm area (Fig. 7a, see from the right). No other significant mineralogical
369 alterations could be observed in the 0.5–5 mm area, which also agrees with the SEM observations (Fig. 3, Fig. 5,
370 and Fig. 6c). The XRD analyses did not include the outer surface (~0.5 mm) and thus no Mg-bearing product, e.g.,
371 brucite, was detected. No brucite deposits could be found in the anodic solution, either.

372

373 The XRD results are also confirmed by TGA, as detailed in Supplementary Data.

374

375 *3.2 Test results of Na₂SO₄ exposure*

376 3.2.1 Chemical composition and microstructural alterations

377

378 Near the cathode, an exposure to Na₂SO₄ in the presence of applied electric fields also induced an increased S
379 content (Fig. 8, see from the left), but to a much lower extent compared with the situation of the MgSO₄ exposure
380 (Fig. 3). The S content in the 0.5–10 mm area after 28 d exposure to Na₂SO₄ (Fig. 8b) was even lower than that of
381 the same area exposed to MgSO₄ for 7 d (Fig. 3a). Different from the situation of MgSO₄ exposure, the loss of Ca²⁺
382 in this area could not be clearly observed. After an exposure time of 28 d, the Ca content on the surface even
383 showed a small increase (Fig. 8b). The microstructure of the cement paste after the exposure to Na₂SO₄ showed
384 different features compared with that of the MgSO₄ exposure. The cement paste in the 0–600 μm area was porous
385 (Fig. 9a). Portlandite and large ettringite crystals could be observed (Fig. 9b). A calcite shell covered the surface of
386 the specimen, and calcite could also be found inside the cement paste.

387

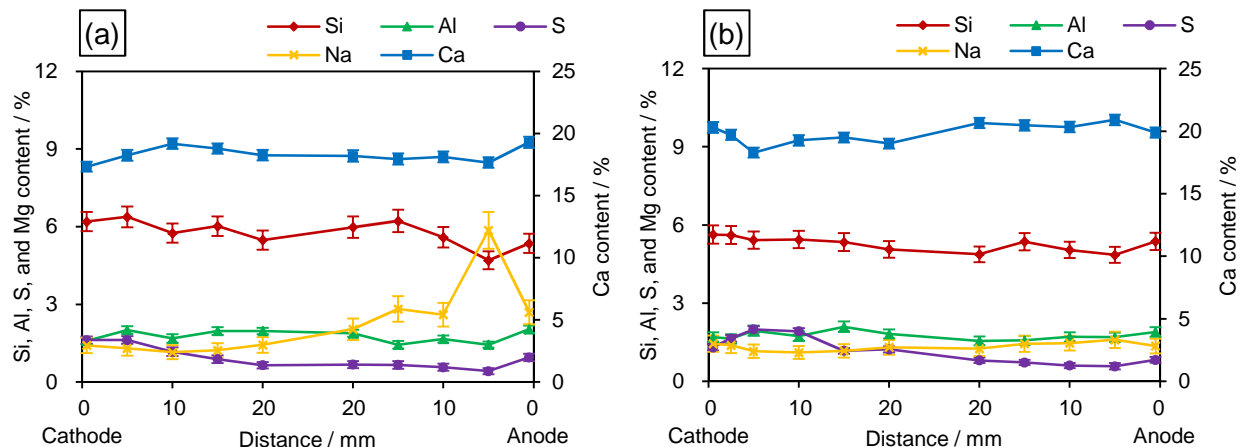


Fig. 8. Chemical composition at different distances from the surface (cathode on the left and anode on the right) after exposure to Na_2SO_4 for (a) 7 d and (b) 28 d.

388

389

390

391

The surface area near the anode (0.5 mm) showed slightly higher S content compared with the areas inside the specimen (Fig. 8, see from the right), which is similar to the situation of MgSO_4 exposure. Different from Mg^{2+} whose penetration depth is less than 100 μm , Na^+ could penetrate deeper into the specimen from the anode, as indicated by its increased content at a depth of 5–15 mm near the anode in Fig. 8a. There are two possible causes for the Na enrichment: a) a continuous accumulation during seven days, or b) a quick accumulation during the day before testing, after the sulfate solution was just refreshed. When we chose not to refresh the solution on the 27th day, no Na enrichment was observed in the specimen on the 28th day (Fig. 8b). This observation supports the second hypothesis and indicates that the migration of Na^+ under electric fields was fast. The microstructure of the surface area after Na_2SO_4 exposure showed some similar features compared with that of MgSO_4 exposure. A CaSO_4 -rich zone also formed (Fig. 10a), and silica gel that is rich in Na can be observed (Spot A of Fig. 10b). Between the CaSO_4 -rich zone and the cement paste, there is a Na-bearing rim (Spot B of Fig. 10b). Comparing the chemical composition of the rim with that of the Na-rich silica gel, the former owned a slightly lower Na content and a higher Ca content. Next to the CaSO_4 -rich zone, the Ca/Si ratio of the hydration products was also higher than 1.5. The Ca/Si ratio became stable beyond this depth ($\sim 100 \mu\text{m}$), as also verified in Fig. 8b.

406

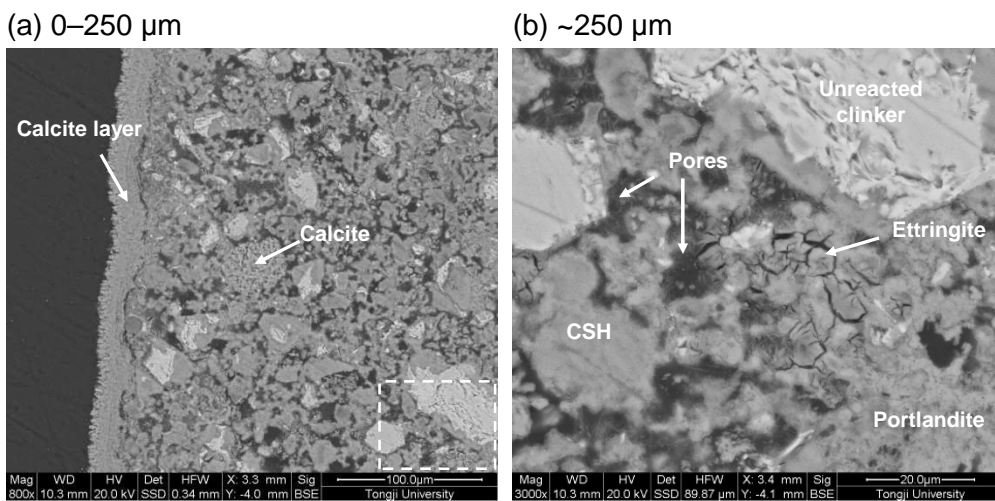


Fig. 9. Microstructure of the surface area (0–250 μm) near the cathode after 28 d exposure to Na_2SO_4 : (a) an overview and (b) enlargement of the squared area. Surface on the left.

410

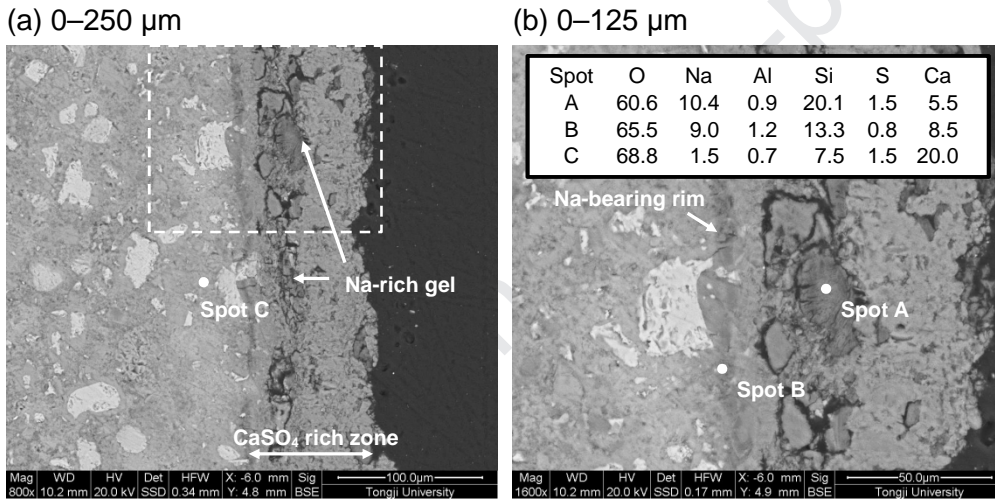


Fig. 10. Microstructure of the surface area (0–250 μm) near the anode after 28 d exposure to Na_2SO_4 : (a) an overview and (b) enlargement of the squared area. Surface on the right.

414

415 The S/Ca plotted against Al/Ca indicates the presence of ettringite in large amounts at 0.5 mm and 5 mm depths
416 from the cathode when the specimen is exposed to Na_2SO_4 for 7 d (Fig. 11a). After an exposure time of 28 d,
417 ettringite was suggested to form at 0.5 mm, 5 mm, and 15 mm depths from the cathode (Fig. 11b), whilst a small
418 amount of ettringite may also be present at the 0.5 mm area from the anode (Fig. 11c).

419

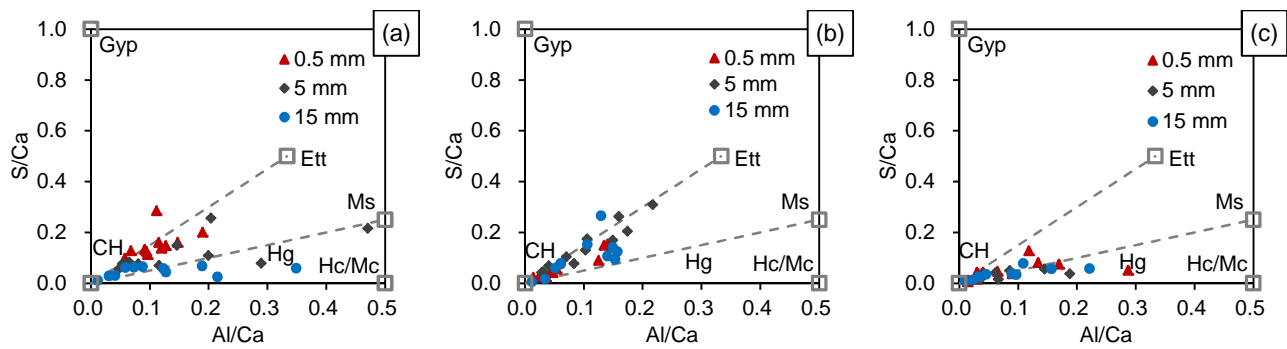


Fig. 11. Atom ratio plots of S/Ca against Al/Ca at different depths from the surface after exposures to Na_2SO_4 : (a) and (b) the cathode areas exposed to Na_2SO_4 for 7 d and 28 d, respectively; (c) the anode areas exposed to Na_2SO_4 for 28 d. CH = Portlandite (and C-S-H at a similar position), Ett = Ettringite, Ms = Monosulfate, Hc/Mc = Hemicarbonate or monocarbonate, Gyp = CaSO_4 .

420

421

422

423

424

425

426

427

428

429

430

431

432

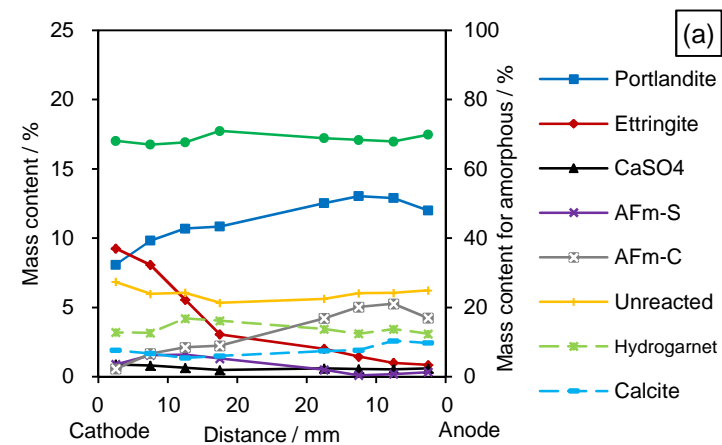
433

434

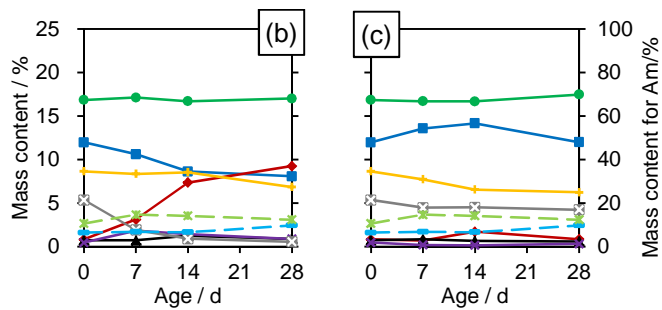
3.2.2 Mineralogical alteration

427

When the specimen is exposed to Na_2SO_4 , CaSO_4 did not form in large amounts near the cathode (e.g., 0.5–20 mm, Fig. 12a, see from the left) even after an exposure time of 28 d. Instead, the ettringite content in this area was high, and it decreased with the distance from the surface. Furthermore, the decomposition of portlandite and AFm (especially monocarbonate and hemicarbonate) after Na_2SO_4 exposure was not as significant as the situations in the MgSO_4 exposure (comparing Fig. 12a to Fig. 7a). The decomposition of portlandite and AFm, and the formation of ettringite showed a positive relationship with time (Fig. 12b).



435



436

437 **Fig. 12.** Mineralogical composition of the specimen exposed to Na_2SO_4 obtained by XRD and Rietveld refinement:
438 (a) all the depths after 28 d exposure time; (b) and (c) phase alteration of the 0.5–5 mm area near the cathode and
439 anode, respectively, after different exposure time. CaSO_4 = anhydrite + bassanite + gypsum, AFm-S = monosulfate,
440 AFm-C = monocarbonate + hemicarbonate, hydrogarnet = katoite + hydrogrossular.

441

442 In the surface area near the anode (0.5–5 mm), no significant mineralogical alterations could be observed except for
443 a small increase in the ettringite content and a decrease in the contents of monocarbonate and hemicarbonate.
444 Similar to the situation of MgSO_4 exposure, these phenomena are assigned to the effects of SO_4^{2-} diffusing from the
445 anodic solution (Fig. 12c). The Na enrichment after 7 d exposure to Na_2SO_4 did not form any products that can be
446 detected by XRD. Moreover, no deposits formed in the cathodic and anodic solutions.

447

448 3.3 Results of thermodynamic modeling

449

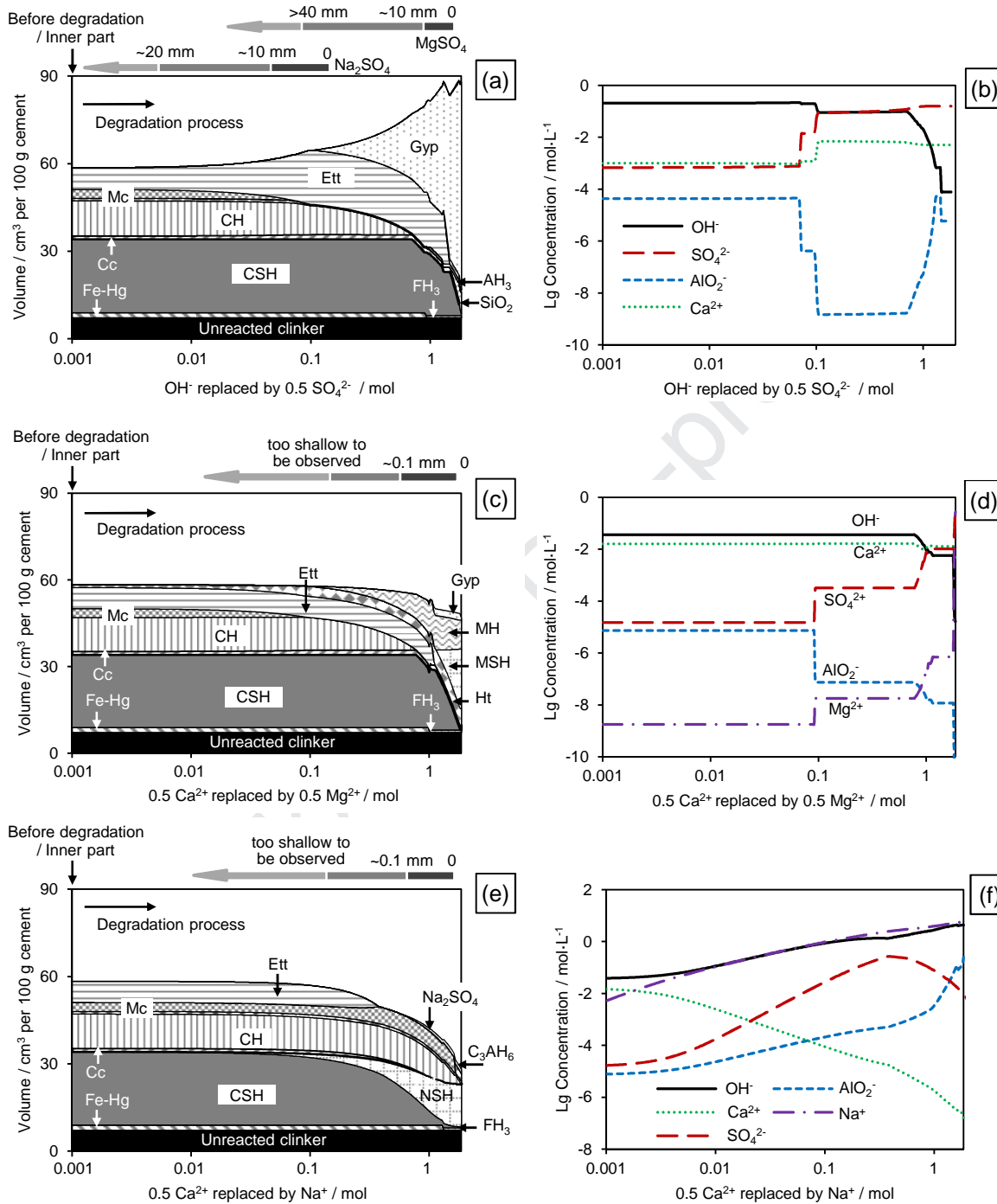
450 3.3.1 Phase assemblage and pore solution chemistry

451

452 The phase assemblage and pore solution chemistry during the simplified electric migration processes were
453 calculated by thermodynamic modeling. For the electric migration near the cathode (Fig. 13a), SO_4^{2-} initially
454 stabilized ettringite in favor of monocarbonate. After the complete consumption of monocarbonate, gypsum was
455 stabilized in favor of portlandite and C-S-H. During these processes, the SO_4^{2-} concentration in the pore solution
456 showed an increase, whilst the OH^- concentration kept decreasing (Fig. 13b). In addition to gypsum, amorphous

457 SiO₂ and AH₃ were predicted as the stable phases at the last stage of the electric migration process.

458



459

460

461

462 **Fig. 13.** Phase assemblage and pore solution chemistry during the simplified electric migration process, calculated
463 by thermodynamic modeling: (a) and (b) the degradation process near the cathode; (c) and (d) the degradation
464 process near the anode after MgSO₄ exposure; (e) and (f) the degradation process near the anode after Na₂SO₄
465 exposure. The horizontal-axis can be interpreted into the alteration in a certain position with time or the distribution
466 of products after a certain exposure time. A logarithmic axis is used for better comparison with thermodynamic
467 modeling studies on diffusion-induced sulfate attacks [1,2,11,14-16]. The arrows above the figures illustrate the

468 approximate distribution of hydration products after 28 d exposure time (experimental results). CH = portlandite,
 469 Ett = ettringite, Mc = monocarbonate, Gyp = gypsum, Cc = calcite, Fe-Hg = $C_3FS_{0.84}H_{4.32}$ and/or $C_3F_{1.34}H_{3.32}$, Ht =
 470 hydrotalcite, MH = brucite, MSH = M-S-H gel, and NSH = the Na end-member, $[(NaOH)_{2.5}SiO_2H_2O]_{0.2}$ included
 471 in the CSHQ model.

472

473 In the anode area exposed to $MgSO_4$ (Fig. 13c), the incorporated Mg^{2+} stabilized hydrotalcite and ettringite in favor
 474 of monocarbonate at an initial stage. Brucite formed when all the monocarbonate was consumed, during which
 475 portlandite decomposed. At the last stage of the electric migration process, M-S-H and gypsum were stabilized in
 476 favor of C-S-H and ettringite, respectively. In contrast, exposure to Na_2SO_4 induced continuous Na uptake in the
 477 C-S-H (Fig. 13e). By separating the Na end-member from the C-S-H phase in the CSHQ model, the Na uptake can
 478 be clearly observed. Portlandite kept stable until the depletion of C-S-H. Ettringite and monocarbonate were
 479 predicted to destabilize during the electric migration process.

480

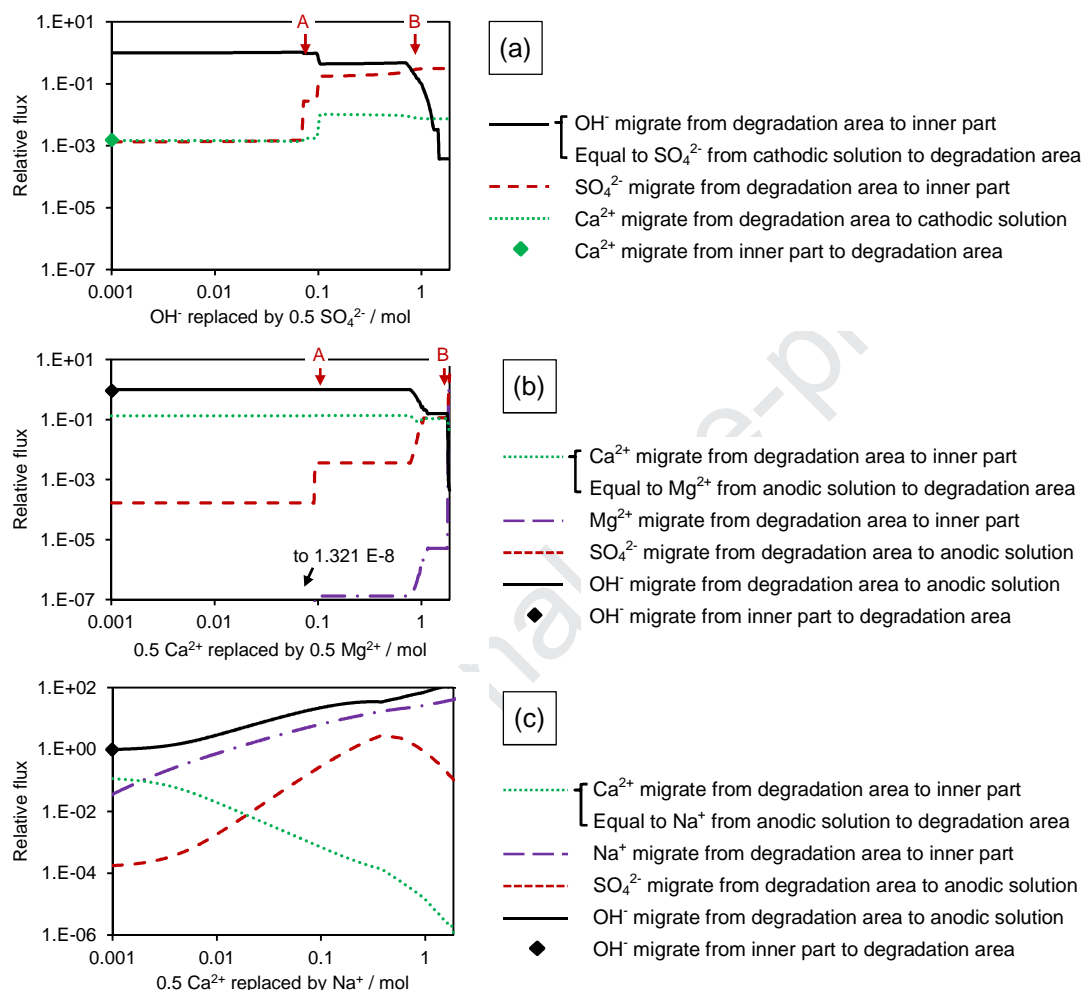
481 3.3.2 Migration of ionic species

482

483 The simplified electric migration process assumes that the phase changes are restricted in a certain “degradation
 484 area” on the surface of a specimen (see Fig. 1b). The relative flux of a certain ion is thus interpreted as its migration
 485 rate from the degradation area towards a certain direction which depends on the ion’s polarity. In the degradation
 486 area near the cathode, when degradation initiated OH^- had the highest relative flux among all the ionic species (Fig.
 487 14a). This phenomenon demonstrates that the replacement of OH^- by SO_4^{2-} from the external solution was the most
 488 significant process that occurred. The relative flux of SO_4^{2-} turned higher when all the monocarbonate decomposed
 489 (point A), and exceeded that of OH^- when portlandite started to decompose and gypsum started to form (point B).
 490 From this point on, SO_4^{2-} would take the place of OH^- as the main ionic species that migrated towards the inner part
 491 of the specimen. The replacement of OH^- by SO_4^{2-} in the degradation area, represented by the relative flux of OH^- ,

492 thus slowed down, and the degradation remained stable at point B. During the degradation process, the relative flux
 493 of Ca^{2+} showed an increase (point A), indicating that the loss of Ca^{2+} from the degradation area to the external
 494 solution will be faster than the compensation from the inner part of the specimen.

495



496
 497
 498 **Fig. 14.** The relative flux of ionic species: (a) the cathode area; (b) and (c) the anode area exposed to MgSO_4 and
 499 Na_2SO_4 , respectively. The cations and anions migrate in different directions, see Fig. 1b. Certain ionic species are
 500 compensated by those from the inner part of the specimen, and the compensation rate is marked by a diamond
 501 (provided that the ionic strength in the inner part of the specimen remains stable). The square bracket indicates the
 502 ionic species in the external solution is transported into the degradation area with the same relative flux to certain
 503 ions based on the assumption of charge balance.
 504

505

506 For the anode area that is exposed to MgSO_4 (Fig. 14b), the relative flux of OH^- remained the highest for a long
 507 period during the electric migration process. This phenomenon indicates that the outflow of OH^- to the external

508 solution, as well as the compensation of OH⁻ from the inner part, was faster than the migration of all the other ions.
 509 The relative flux of Ca²⁺ was at a lower level, indicating that the Ca²⁺ in the degradation area would be replaced by
 510 the Mg²⁺ from the external solution at a slow rate. The relative flux of Mg²⁺ was even lower than that of Ca²⁺,
 511 indicating that the Mg²⁺ in the degradation area could hardly migrate towards the inner part. The relative flux of
 512 SO₄²⁻ showed an increase during the electric migration process (point A). This phenomenon will theoretically lead
 513 to a loss of SO₄²⁻ in the degradation area, but this effect may be offset by the diffusion of SO₄²⁻ from the external
 514 solution in the experiments. At the last degradation stage (point B), the relative flux of Mg²⁺ increased sharply, the
 515 penetration of Mg²⁺ started, and the entire electric migration process repeated stepwise in a slightly deeper area
 516 from the surface. The degradation phase assemblage thus kept stable at point B.

517

518 When the anode was exposed to Na₂SO₄ (Fig. 14c), the relative flux of OH⁻ remained the highest among all the
 519 ionic species during the entire electric migration process. The relative flux of Na⁺ was lower than that of OH⁻, but
 520 much higher than that of Mg²⁺ in the specimen exposed to MgSO₄. This phenomenon indicates that Na⁺ will
 521 migrate into the cement paste at a much higher rate than Mg²⁺. The relative flux of Ca²⁺ was at a low level during
 522 the electric migration process, suggesting that the replacement of Ca²⁺ by Na⁺ in the degradation area will be slow,
 523 and most Na⁺ will migrate towards the inner part of the specimen.

524

525 **4 Discussions**

526 *4.1 Comparison between test results and thermodynamic modeling*

527

528 The mineralogical alterations that occurred near the cathode agreed well with the thermodynamic modeling, as
 529 indicated by the arrows in Fig. 13a. After exposure to MgSO₄ for 28 d, CaSO₄ was observed to form in the outer

530 part of the specimen (0–10 mm) where almost no portlandite or ettringite existed (XRD, Fig. 7a). The
 531 silica-alumina gel found on the surface of the specimen (SEM, Fig. 4b) corresponds to the amorphous SiO₂ and
 532 AH₃ in the thermodynamic modeling [14], and the reduction of the amorphous content coincides with the
 533 decomposition of C-S-H predicted by thermodynamic modeling. Deeper inside the specimen (10–40 mm), the
 534 content of CaSO₄ gradually decreased, while those of portlandite and ettringite increased (XRD, Fig. 7a). In
 535 comparison, the specimen exposed to Na₂SO₄ for 28 d remained at an earlier degradation stage, when CaSO₄ did
 536 not form in large amounts. The different degradation stages between the specimens also coincide with the amount
 537 of S that has been transported from the cathodic solution into the cement paste (EDS, cf. Fig. 3b and Fig. 8b).

538

539 The mineralogical alterations occurred in a shallow depth (~0.1 mm) in the cement paste near the anode, but had
 540 proceeded to the last degradation stage in both exposure conditions when comparing the test results with the
 541 thermodynamic modeling (Fig. 13c and 13e). For the MgSO₄ exposure, the presence of Mg-containing products
 542 (brucite and M-S-H, SEM, Fig. 5) agrees with the thermodynamic calculation, while for the Na₂SO₄ exposure, the
 543 Na-rich silica gel (Fig. 10) coincides with the Na uptake by C-S-H in the thermodynamic modeling. A CaSO₄-rich
 544 zone was observed in both exposure conditions no matter if CaSO₄ is predicted to be stable. The diffusion of SO₄²⁻
 545 from the anodic solution is believed to be responsible for this phenomenon (see also Fig. 1b).

546

547 *4.2 Migration behavior of Mg²⁺, Na⁺, and SO₄²⁻*

548

549 The degradation near the cathode and anode proceeded in different ways. Near the cathode, the anions from the
 550 external solution (mainly SO₄²⁻) migrated into a deep area, and the mineralogical alteration proceeded gradually
 551 following the prediction of thermodynamic modeling. For the anode area exposed to MgSO₄, the incorporation of

552 Mg^{2+} occurred in a shallow area with the mineralogical alteration proceeding directly to the late degradation stage.

553 In contrast, Na^+ could penetrate deep into the cement paste, but the mineralogical alteration occurred also in a

554 shallow area. The different migration behaviors of the ionic species can be explained by the relative flux which is

555 obtained from the solution chemistry calculated by thermodynamic modeling.

556

557 According to section 3.3.2, an ion's capability for migration under electric fields depends on its relative flux, while

558 its accumulation rate in a degradation area depends on the relative flux of the other ion that is being replaced. For

559 the degradation process near the cathode, the high relative flux of OH^- suggests a fast accumulation of SO_4^{2-} at an

560 early degradation stage, whilst the increased relative flux of SO_4^{2-} indicates an accelerated migration rate towards

561 the inner part of the specimen (Fig. 14a). In contrast, for the degradation process near the anode, the smaller

562 relative flux of Ca^{2+} than that of OH^- suggests a slower accumulation rate of the cations (Mg^{2+} or Na^+) than the

563 outflow of OH^- (Fig. 14b and 14c), which coincides with the shallow depth of Mg^{2+} and Na^+ incorporation (Fig. 5

564 and 10). The strengths of Na^+ and Mg^{2+} in the pore solution (Fig. 13d and 13f) and thus their relative fluxes (Fig.

565 14b and 14c) were different after the chemical reactions. As a result, Na^+ and Mg^{2+} showed different migration

566 behaviors (also compare Fig. 3 and Fig. 8). The different migration behaviors of SO_4^{2-} and Mg^{2+} were once realized

567 when using thermodynamic modeling to study the magnesium sulfate attack simply caused by diffusion [15,16]. It

568 was reported that the penetration depth of Mg^{2+} is usually overestimated compared to that of SO_4^{2-} . According to

569 the findings in this paper, this can be explained by the low concentration of Mg^{2+} in the pore solution and thus its

570 slower diffusion rate than SO_4^{2-} .

571

572 The electric migration of the cations and anions can also influence each other because both processes carry electric

573 charges. The experiment was conducted under a constant electric current. The same amount of charges should pass

574 through the specimen during the same period of time, no matter the specimen was exposed to $MgSO_4$ or Na_2SO_4 . In
 575 the cathode side, SO_4^{2-} was migrated from the cathodic solution into the cement paste. It penetrated through the
 576 specimen together with OH^- (and other anions) in the pore solution. In the meanwhile, the Ca^{2+} in the pore solution
 577 were released into the cathodic solution, but this process carried less electric charges due to the low relative flux of
 578 Ca^{2+} than the anions. In the anode side exposed to $MgSO_4$, the migration of Mg^{2+} and Ca^{2+} towards the inner part of
 579 the specimen were at low rates. The electric charges were mainly carried by the OH^- migrating from the inner part
 580 of the specimen towards the anode side, and finally into the anodic solution. In contrast, in the case of Na_2SO_4
 581 exposure, Na^+ could penetrate through the specimen much more easily than Mg^{2+} , and its electric migration can
 582 carry much more electric charges. Under such circumstance, the electric migration of anions (SO_4^{2-} and OH^-) will
 583 carry fewer charges, and thus the sulfate ingress will proceed on a lower rate compared with the situation of $MgSO_4$
 584 exposure. Similar results were also reported in [41] but no convincing explanations were ever given.

585

586 *4.3 Comparison with the sulfate attack induced by diffusion*

587

588 To compare with the sulfate attack in the absence of electric field (induced by diffusion), the main mineralogical
 589 alterations of Portland cement (Type I with limestone addition) mortars under Na_2SO_4 and $MgSO_4$ attacks [11,15]
 590 and the results obtained in this paper are summarized in Table 3. This section focuses on the sulfate ingress and
 591 decalcification near the cathode because a) these effects influenced a much wider area than the phase alterations
 592 near the anode and b) similar processes also occur in the diffusion-induced sulfate attacks.

593

594 In the diffusion-induced Na_2SO_4 attack, the ingress of sulfate leads to the formation of ettringite followed by that of
 595 gypsum. In the $MgSO_4$ attack, nevertheless, Mg^{2+} reacts with OH^- in the pore solution to form brucite, reducing the

596 solution pH to ~10.5 and inducing the decomposition of ettringite [60,61]. The decomposition of ettringite was also
 597 observed here when the specimen is exposed to $MgSO_4$. This phenomenon can be also attributed to a reduction of
 598 the pore solution alkalinity, but the presence of Mg^{2+} may not be a decisive factor considering the shallow depth of
 599 the Mg transportation (Fig. 3b). During the sulfate ingress, the OH^- in the pore solution near the cathode was
 600 theoretically transported towards the inner part of the specimen by the electric field. This process is used as a basic
 601 assumption in the thermodynamic modeling and it is shown that the decomposition of ettringite and the formation
 602 of gypsum occurred simultaneously with the decrease of OH^- concentration in the pore solution (Fig. 13b).
 603 According to the test results, the presence of $CaSO_4$ in the cement paste near the cathode (Fig. 7) indicates
 604 sufficient ionic strengths of Ca^{2+} and SO_4^{2-} for the stabilization of ettringite [2,14,15], whilst the Al content in the
 605 hydration products did not show any apparent reduction (Fig. 3). It can be thus inferred that the decomposition of
 606 ettringite was most probably caused by a neutralization process as assumed in the thermodynamic modeling. A
 607 similar neutralization process was also observed when accelerating thaumasite sulfate attacks by applied electric
 608 fields, and this process was also believed to destabilize ettringite according to [62].
 609

610 **Table 3** Mineralogical alterations of sulfate attacks induced by electric migration (this paper) and diffusion
 611 (obtained from [11,15]).

Process	Formation phase	Decomposition phase
Electric migration, cathode	Ettringite → Gypsum + Si-Al gel	Monocarbonate → Portlandite → Ettringite → C-S-H
Electric migration, anode, Na_2SO_4 ¹	Na-rich silica gel + Gypsum (surface)	Not clearly observed in the experiments
Electric migration, anode, $MgSO_4$ ¹	M-S-H + Brucite + Gypsum (surface)	Not clearly observed in the experiments
Diffusion, Na_2SO_4	Ettringite → Gypsum ²	Monocarbonate → Portlandite → C-S-H
Diffusion, $MgSO_4$	Ettringite → Brucite → Gypsum → M-S-H	Monocarbonate → Portlandite → Ettringite → C-S-H

612 ¹ Only the experimentally verified phases are listed in the formation column. The decomposition order of the hydration products was
 613 not clearly observed in the experiments and thus is not listed in the decomposition column.

614 ² Gypsum forms when the Na_2SO_4 concentration is high, e.g., 44 g/L in [11].

615

616 In the diffusion-induced sulfate attack, decalcification usually occurs on the surface of a specimen and is

617 characterized by the decomposition of portlandite and the decrease of the Ca/Si in C-S-H [1,63,64]. In the presence
 618 of bicarbonate, gypsum will be the only stable sulfate-bearing product in the decalcification zone, and amorphous
 619 SiO₂ and AH₃ are predicted as the stable phases by thermodynamic calculation [14,15]. Similar results are also
 620 obtained in this paper (e.g., the MgSO₄ exposure for 28 d), but a different mechanism can be proposed when the
 621 decalcification is induced by electric migration. According to the thermodynamic modeling, the relative flux of
 622 Ca²⁺ migrating from the cement paste to the external solution accelerated during the degradation process (Fig. 14a).
 623 This suggests that the loss of Ca²⁺ in the cement paste near the cathode cannot be fully compensated by the Ca²⁺
 624 migrating from the inner part of the specimen. The Ca²⁺ content near the cathode decreased (Fig. 3 and 8), thus
 625 leading to the decalcification and the decomposition of hydration products. The decalcification near the cathode
 626 may also have accelerated the transportation of Mg²⁺ through diffusion (Fig. 3b and Fig. 4c), as also reported in
 627 concrete exposed to field conditions [65,66]. But the presence of Mg is not likely to be the cause of decalcification
 628 here considering the depths of these processes (Fig. 4, Area III showed decalcification but very small Mg content).

629

630 The Ca/Si ratio (cf. Fig. 3 and Fig. 8) and portlandite content (cf. Fig. 7 and Fig. 12) indicate that the specimen
 631 exposed to MgSO₄ had a higher degree of decalcification than that exposed to Na₂SO₄. On one hand, the
 632 decalcification process is induced by the electric migration of Ca²⁺. It will be impacted by the electric migration of
 633 other cations (Mg²⁺ and Na⁺), and thus the degree of decalcification coincides with that of sulfate ingress. On the
 634 other hand, this process is also impacted by alterations of ionic strength in the external sulfate solution near the
 635 cathode, which is a potential drawback of the test setup. When the specimen was exposed to Na₂SO₄, H⁺ in the
 636 solution would be reduced to H₂ on the cathode, thus producing OH⁻ in the solution [40] (Fig. 1b). Both OH⁻ and
 637 SO₄²⁻ could carry electric charges and would migrate into the cement paste near the cathode. The OH⁻ migrating
 638 towards the specimen may react with the Ca²⁺ that was driven out of the paste to form a surface layer consisting of

639 portlandite. When the Na₂SO₄ solution was refreshed (every 3 d), the portlandite might carbonate, forming a calcite
640 layer as observed in the SEM (Fig. 9). This hypothesis explains the slight increase of the Ca content near the
641 cathode area in Fig. 8b and a better protection from carbonation may help with its verification. In contrast, in the
642 MgSO₄ solution, the OH⁻ produced on the cathode precipitated with Mg²⁺ to form brucite in the external solution
643 (section 3.1.2). Owing to the precipitation of OH⁻, SO₄²⁻ was the main anion migrating into the specimen, and thus
644 CaSO₄ formed on the surface of the specimen instead of calcite (Fig. 4b).

645

646 *4.4 Comparison with coupled reactive-transport modeling*

647

648 As stated in [1], the coupled reactive-transport modeling and the pure thermodynamic modeling presented
649 comparable results in revealing the phase alterations of a diffusion-induced sulfate attack. The pure thermodynamic
650 modeling is usually easy to use and provides fast results, but the results do not correspond directly with the real
651 exposure time or the depth from the exposure surface. In comparison, coupled reactive-transport modeling provides
652 the information of time and depth, but the accuracy depends strongly on the preciseness of models (e.g.,
653 transportation equation, fluid transport, charge balance) [21,67] and parameters (e.g., diffusion coefficient) [1]. This
654 paper proposed a simplified approach for the pure thermodynamic modeling study of electric-migration-induced
655 sulfate attacks. Such an approach focuses on the chemical and mineralogical aspects and clarifies alterations of the
656 hydration products. Although the real distribution of the products was not presented, this information can be
657 reflected by the relative flux that is proposed here. The advantages and validity of this approach will be further
658 demonstrated in an upcoming paper investigating the effect of supplementary cementitious materials in the same
659 situation.

660

661 The thermodynamic modeling calculation conducted in this paper is based on the assumption that the kinetics of the
662 chemical reactions is much faster than the transportation of ionic species, and that the hydration system is close to
663 an equilibrium state. As reviewed in [68], this assumption is usually valid in most practical cases involving the
664 diffusion of ions in saturated systems, and thus it is widely accepted by the existing pure thermodynamic modeling
665 studies [1,2,11,14-16]. In contrast, electric migration usually induces a quicker ionic motion, and thus the
666 equilibrium state is more difficult to be reached [24]. When studying the electric migration of chloride by coupled
667 reactive-transport models, an equilibrium state was assumed in [69] and the test results agree well with the
668 modeling. The results of this paper also show that the migration behavior of ionic species coincides with the
669 solution chemistry (relative flux) under the assumption of equilibrium. It can be thus inferred that the real solution
670 chemistry in the hydrated cement paste is similar to that under the equilibrium state and that the equilibrium
671 assumption is likely to be valid in the case of electric migration.

672

673 The electric migration behavior of ionic species can be represented by the relative flux, which depends on the ion's
674 diffusion coefficient and concentration in the pore solution. The diffusion coefficients of different ions are usually
675 at the same order of magnitude, as shown in Table 2. However, their concentrations can span several orders of
676 magnitude, which induces wide differences in the relative fluxes and is responsible for the different migration
677 behavior of Mg^{2+} , Na^+ , and SO_4^{2-} under applied electric fields. In this respect, for a reactive-transport process, it is
678 sometimes acceptable to suppose the same diffusion coefficient for different ionic species, as was done in
679 [16,70,71]. Nevertheless, the effect of chemical reactions on the concentration and thus the migration of ionic
680 species should be carefully considered.

681

682 *4.5 Comparison with real-life situations*

683

684 This setup simulates both processes when electric current flows into and out of the cement-based materials
685 simultaneously. In contrast, in the case of DC stray current, these two processes occur separately. The electric
686 current enters the concrete at a certain location, goes through the reinforcement, and then flows out of the concrete
687 at another location [29]. The ionic exchange between the external environment and cement-based materials induced
688 by the inflow and outflow of electric current can be represented by the anode area and cathode area in this setup,
689 respectively, but the behavior of the reinforcements, e.g., anodic corrosion or hydrogen evolution, is not simulated.
690 Moreover, this paper focused on the chemical and mineralogical aspects of sulfate attacks and thus the physical and
691 microstructural aspects, including expansion and cracking, were not investigated. During the electric migration
692 tests, the specimens did not show significant cracking, which agrees with the focus of this paper but may possibly
693 differ from the real situation. The test results (Fig. 7) and thermodynamic modeling (Fig. 13a) both indicate the
694 decomposition of ettringite at the late degradation stage, probably suggesting the absence of expansion at that stage.
695 However, thermodynamic modeling predicted an increased volume of hydration products near the cathode, which
696 may yet cause expansion. Based on the results of this paper, it is difficult to determine whether expansion and
697 cracking will occur under such circumstances.

698

699 The concentration of ions in the external solution will change with time, and this will be the other difference
700 between the test setup and the real-life situation. Although the concentration of the sulfate solution theoretically
701 remains above ~0.34 mol/L due to the 3-day periodically refreshment (see section 2.2 and Supplementary Data), it
702 seems that the alterations of the ionic strength in the external sulfate solution have still impact the products formed
703 on the surface of the specimens (see section 4.3). Increasing the volume of the external solutions and shortening the
704 refreshing cycle can be solutions to this problem.

705

706 The test setup used here has been proposed for the purpose of laboratory acceleration tests [39-41]. The discussion
707 in section 4.3 demonstrates that the electric migration of ionic species near the cathode not only induce the ingress
708 of sulfate, but also cause a neutralization process in the pore solution and a decalcification process (see also Table
709 3). These effects should be considered when interpreting the mineralogical alterations obtained by such test setups,
710 especially when a) MgSO₄ attack is investigated and the degradation proceeds to the late-stage quickly and b) a
711 long exposure time is investigated in the case of Na₂SO₄ attack and the degradation may proceed to a later stage
712 compared with that in this paper. After an exposure time of 28 d, SO₄²⁻ from the cathodic solution had penetrated
713 through most of the specimen and even influenced the area that is 5–10 mm deep from the anode, as indicated by
714 the distribution of hydration products (Fig. 7 and Fig. 12). Specimens with greater height are thus recommended for
715 such tests, especially in the case of long duration (e.g., > 28 d exposure time), in order that the real penetration
716 depth of SO₄²⁻ can be accurately identified from an uncontaminated area.

717

718 In addition to the situations mentioned above, we believe that the simplified approach for the thermodynamic
719 modeling study proposed in this paper can be more broadly applied in investigating the behavior of cement-based
720 materials under applied electric fields. Future studies may involve the use of this approach in accelerated
721 electrochemical leaching tests [37,38], other types of chemical attacks, and in concrete technologies involving
722 electrochemical methods (e.g., chloride extraction, realkalinization, and electrochemical deposit [32-34]).

723

724 **5 Conclusions**

725

726 When an electric current flows out of a Portland cement paste (in the cathode area of the specimen), the electric

727 migration of ionic species induced the ingress of sulfate from the external solution. Ettringite formed at the initial
728 stage but decomposed to form gypsum at a later stage. Thermodynamic modeling indicates that the alkalinity of the
729 pore solution decreased during this process, which is most probably responsible for the decomposition of ettringite.

730 In addition to the sulfate ingress, decalcification also occurred in this area, which is characterized by the
731 decomposition of portlandite followed by that of C-S-H. When the specimen was exposed to MgSO₄, the sulfate
732 ingress and decalcification proceeded to a later stage and occurred in a deeper area compared with the specimen
733 exposed to Na₂SO₄.

734

735 Near the anode, electric current flows into the cement paste, and the electric charges were mainly carried by the
736 electric migration of OH⁻ from the pore solution towards the external solution. The Ca²⁺ originally in the pore
737 solution migrated towards the inner part of the specimen at a much lower rate than that of OH⁻, and thus the
738 incorporation of the cations from the external solution (Mg²⁺ or Na⁺) was slow. The incorporation of Mg²⁺ formed
739 brucite and M-S-H-like products. Thermodynamic modeling indicates that this process induced a low Mg²⁺
740 concentration in the pore solution, and thus Mg²⁺ would not effectively migrate into the inner part of the specimen.

741 In contrast, the incorporation of Na⁺ formed Na-rich silica gel, during which the Na⁺ concentration in the pore
742 solution was much higher. As a result, Na⁺ showed a better capability of migration and can penetrate through the
743 cement paste easily. Since both cations and anions can carry electric charges, the different migration behaviors of
744 Mg²⁺ and Na⁺ are attributed to inducing the different degrees of sulfate ingress near the cathode.

745

746 A simplified approach based on thermodynamic modeling and the ionic transportation equation were newly
747 proposed to provide insights into the degradation processes of the sulfate attacks that are induced by electric
748 migration. In addition to calculating the degradation phase assemblage, the migration behavior of ionic species

749 under electric fields can be represented by the relative flux. We believe this approach can be more broadly applied
750 to predict the behavior of cement-based materials under electric fields.

751

752 **Acknowledgements**

753

754 The authors gratefully acknowledge the financial supports provided by National Key Research and Development
755 Projects (2018YFC0705404), National Natural Science Foundation of China (51878480, 51678442, 51878481, and
756 51878496), and the Fundamental Research Funds for the Central Universities.

757

758 **Appendix A. Supplementary Data**

759

- 760 1 Estimating the concentration range of the sulfate solution
761 2 Rietveld refinement
762 3 Input recipes for thermodynamic modeling
763 4 Mineralogical alterations of cement paste tested by TGA

764

765 **References**

766

- 767 [1] B. Lothenbach, B. Bary, P. Le Bescop, T. Schmidt, N. Leterrier, Sulfate ingress in Portland cement, Cem. Concr. Res.
768 40 (2010) 1211-1225.
769 [2] W. Kunther, B. Lothenbach, K.L. Scrivener, On the relevance of volume increase for the length changes of mortar
770 bars in sulfate solutions, Cem. Concr. Res. 46 (2013) 23-29.

- 771 [3] M. Whittaker, L. Black, Current knowledge of external sulfate attack, *Adv. Cem. Res.* 27 (2015) 532-545.
- 772 [4] R.J. Flatt, G.W. Scherer, Thermodynamics of crystallization stresses in DEF, *Cem. Concr. Res.* 38 (2008) 325-336.
- 773 [5] R. Flatt, N. Aly Mohamed, F. Caruso, H. Derluyn, J. Desarnaud, B. Lubelli, R.M. Espinosa-Marzal, L. Pel, C.
- 774 Rodriguez-Navarro, G.W. Scherer, N. Shahidzadeh, M. Steiger, Predicting salt damage in practice: A theoretical insight
775 into laboratory tests, *RILEM Technical Letters*. 2 (2017) 108.
- 776 [6] W. Müllauer, R.E. Beddoe, D. Heinz, Sulfate attack expansion mechanisms, *Cem. Concr. Res.* 52 (2013) 208-215.
- 777 [7] C. Yu, W. Sun, K. Scrivener, Mechanism of expansion of mortars immersed in sodium sulfate solutions, *Cem. Concr.*
778 *Res.* 43 (2013) 105-111.
- 779 [8] C. Yu, W. Sun, K. Scrivener, Degradation mechanism of slag blended mortars immersed in sodium sulfate solution,
780 *Cem. Concr. Res.* 72 (2015) 37-47.
- 781 [9] M. Santhanam, M.D. Cohen, J. Olek, Effects of gypsum formation on the performance of cement mortars during
782 external sulfate attack, *Cem. Concr. Res.* 33 (2003) 325-332.
- 783 [10] B. Tian, M.D. Cohen, Does gypsum formation during sulfate attack on concrete lead to expansion?, *Cem. Concr.*
784 *Res.* 30 (2000) 117-123.
- 785 [11] T. Schmidt, B. Lothenbach, M. Romer, J. Neuenschwander, K. Scrivener, Physical and microstructural aspects of
786 sulfate attack on ordinary and limestone blended Portland cements, *Cem. Concr. Res.* 39 (2009) 1111-1121.
- 787 [12] B. Bary, N. Leterrier, E. Deville, P. Le Bescop, Coupled chemo-transport-mechanical modelling and numerical
788 simulation of external sulfate attack in mortar, *Cem. Concr. Compos.* 49 (2014) 70-83.
- 789 [13] A. Soive, V.Q. Tran, External sulfate attack of cementitious materials: New insights gained through numerical
790 modeling including dissolution/precipitation kinetics and surface complexation, *Cem. Concr. Compos.* 83 (2017)
791 263-272.
- 792 [14] W. Kunther, B. Lothenbach, K. Scrivener, Influence of bicarbonate ions on the deterioration of mortar bars in sulfate

- 793 solutions, Cem. Concr. Res. 44 (2013) 77-86.
- 794 [15] W. Kunther, B. Lothenbach, Improved volume stability of mortar bars exposed to magnesium sulfate in the presence
795 of bicarbonate ions, Cem. Concr. Res. 109 (2018) 217-229.
- 796 [16] W. Kunther, B. Lothenbach, K.L. Scrivener, Deterioration of mortar bars immersed in magnesium containing sulfate
797 solutions, Mater. Struct. 46 (2013) 2003-2011.
- 798 [17] Z. Makhloifi, S. Aggoun, B. Benabed, E.H. Kadri, M.Bederina, Effect of magnesium sulfate on the durability of
799 limestone mortars based on quaternary blended cements, Cem. Concr. Compos. 65 (2016) 186-199.
- 800 [18] B. Huber, H. Hilbig, J.E. Drewes, E. Müller, Evaluation of concrete corrosion after short- and long-term exposure to
801 chemically and microbially generated sulfuric acid, Cem. Concr. Res. 94 (2017) 36-48.
- 802 [19] L. Gu, P. Visintin, T. Bennett, Evaluation of accelerated degradation test methods for cementitious composites
803 subject to sulfuric acid attack; application to conventional and alkali-activated concretes, Cem. Concr. Compos. 87 (2018)
804 187-204.
- 805 [20] E. Rozière, A. Loukili, R. El Hachem, F. Grondin, Durability of concrete exposed to leaching and external sulphate
806 attacks, Cem. Concr. Res. 39 (2009) 1188-1198.
- 807 [21] E. Samson, J. Marchand, Modeling the transport of ions in unsaturated cement-based materials, Computers &
808 Structures. 85 (2007) 1740-1756.
- 809 [22] R.A. Patel, Q.T. Phung, S.C. Seetharam, J. Perko, D. Jacques, N. Maes, G. De Schutter, G. Ye, K. Van Breugel,
810 Diffusivity of saturated ordinary Portland cement-based materials: A critical review of experimental and analytical
811 modelling approaches, Cem. Concr. Res. 90 (2016) 52-72.
- 812 [23] P. Yang, G. Sant, N. Neithalath, A refined, self-consistent Poisson-Nernst-Planck (PNP) model for electrically
813 induced transport of multiple ionic species through concrete, Cem. Concr. Compos. 82 (2017) 80-94.
- 814 [24] E. Samson, J. Marchand, K.A. Snyder, Calculation of ionic diffusion coefficients on the basis of migration test

- 815 results, Mater. Struct. 36 (2003) 156-165.
- 816 [25] J.M. Galíndez, J. Molinero, On the relevance of electrochemical diffusion for the modeling of degradation of
817 cementitious materials, Cem. Concr. Compos. 32 (2010) 351-359.
- 818 [26] C. Li, M. Wu, W. Yao, Effect of coupled B/Na and B/Ba doping on hydraulic properties of belite-ye'elite-ferrite
819 cement, Constr. Build. Mater. 208 (2019) 23-35.
- 820 [27] L. Bertolini, M. Carsana, P. Pedferri, Corrosion behaviour of steel in concrete in the presence of stray current,
821 Corros. Sci. 49 (2007) 1056-1068.
- 822 [28] A. Aghajani, M. Urgen, L. Bertolini, Effects of DC stray current on concrete permeability, J. Mater. Civ. Eng. 28
823 (2015) 04015177.
- 824 [29] A. Solgaard, M. Carsana, M. Geiker, A. Küter, L. Bertolini, Experimental observations of stray current effects on
825 steel fibres embedded in mortar, Corros. Sci. 74 (2013) 1-12.
- 826 [30] F. Wittmann, Corrosion of cement-based materials under the influence of an electric field, Mater. Sci. Forum,
827 Trans Tech Publ, 1997, pp. 107-126.
- 828 [31] G. Glass, N. Buenfeld, The inhibitive effects of electrochemical treatment applied to steel in concrete, Corros. Sci.
829 42 (2000) 923-927.
- 830 [32] W.H.A. Peelen, R.B. Polder, E. Redaelli, L. Bertolini, Qualitative model of concrete acidification due to cathodic
831 protection, Mater. Corros. 59 (2008) 81-89.
- 832 [33] Y. Chen, W. Yao, J. Zuo, Effect of ultrasound on electrochemical chloride extraction from mortar, Materials
833 Research Express. 5 (2018) 036508.
- 834 [34] W. Li, B. Dong, Z. Yang, J. Xu, Q. Chen, H. Li, F. Xing, Z. Jiang, Recent Advances in Intrinsic Self-Healing
835 Cementitious Materials, Adv. Mater. 30 (2018) e1705679.
- 836 [35] J. García, F. Almeraya, C. Barrios, C. Gaona, R. Núñez, I. López, M. Rodríguez, A. Martínez-Villafaña, J.M.

- 837 Bastidas, Effect of cathodic protection on steel–concrete bond strength using ion migration measurements, *Cem. Concr.*
- 838 *Compos.* 34 (2012) 242-247.
- 839 [36] J.C. Orellan, G. Escadeillas, G. Arliguie, Electrochemical chloride extraction: efficiency and side effects, *Cem.*
- 840 *Concr. Res.* 34 (2004) 227-234.
- 841 [37] A. Babaahmadi, L. Tang, Z. Abbas, T. Zack, P. Mårtensson, Development of an electro-chemical accelerated ageing
- 842 method for leaching of calcium from cementitious materials, *Mater. Struct.* 49 (2016) 705-718.
- 843 [38] A. Babaahmadi, L. Tang, Z. Abbas, P. Mårtensson, Physical and Mechanical Properties of Cementitious Specimens
- 844 Exposed to an Electrochemically Derived Accelerated Leaching of Calcium, *International Journal of Concrete Structures*
- 845 and Materials.
- 846 [39] Q. Huang, C. Wang, C. Yang, L. Zhou, J. Yin, Accelerated sulfate attack on mortars using electrical pulse, *Constr.*
- 847 *Build. Mater.* 95 (2015) 875-881.
- 848 [40] Q. Huang, C. Wang, C. Luo, C. Yang, Y. Luo, H. Xie, Effect of mineral admixtures on sulfate resistance of mortars
- 849 under electrical field, *Adv. Cem. Res.* 29 (2017) 45-53.
- 850 [41] S. Lorente, M.-P. Yssorche-Cubaynes, J. Auger, Sulfate transfer through concrete: Migration and diffusion results,
- 851 *Cem. Concr. Compos.* 33 (2011) 735-741.
- 852 [42] A. Susanto, D.A. Koleva, O. Copuroglu, K. van Beek, K. van Breugel, Mechanical, electrical and microstructural
- 853 properties of cement-based materials in conditions of stray current flow, *Journal of Advanced Concrete Technology.* 11
- 854 (2013) 119-134.
- 855 [43] K. Scrivener, R. Snellings, B. Lothenbach, A practical guide to microstructural analysis of cementitious materials,
- 856 Crc Press, 2016.
- 857 [44] W. Dollase, Correction of intensities for preferred orientation in powder diffractometry: application of the March
- 858 model, *J. Appl. Crystallogr.* 19 (1986) 267-272.

- 859 [45] R. Snellings, A. Bazzoni, K. Scrivener, The existence of amorphous phase in Portland cements: Physical factors
860 affecting Rietveld quantitative phase analysis, *Cem. Concr. Res.* 59 (2014) 139-146.
- 861 [46] M.A.G. Aranda, A.G. De la Torre, L. Leon-Reina, Rietveld Quantitative Phase Analysis of OPC Clinkers, *Cements*
862 and *Hydration Products*, *Reviews in Mineralogy and Geochemistry*. 74 (2012) 169-209.
- 863 [47] K. Mohan, H. Taylor, Analytical Electron Microscopy of Cement Pastes: IV, β -Dicalcium Silicate Pastes, *J. Am.*
864 *Ceram. Soc.* 64 (1981) 717-719.
- 865 [48] J. Li, G. Geng, R. Myers, Y.-S. Yu, D. Shapiro, C. Carraro, R. Maboudian, P.J.M. Monteiro, The chemistry and
866 structure of calcium (alumino) silicate hydrate: A study by XANES, ptychographic imaging, and wide- and small-angle
867 scattering, *Cem. Concr. Res.* 115 (2019) 367-378.
- 868 [49] J. Kerr, D. Lide, *CRC Handbook of Chemistry and Physics*, CRC Press Boca Raton, FL, USA, 2000.
- 869 [50] J. Xia, L.-y. Li, Numerical simulation of ionic transport in cement paste under the action of externally applied
870 electric field, *Constr. Build. Mater.* 39 (2013) 51-59.
- 871 [51] C. Andrade, R. Buják, Effects of some mineral additions to Portland cement on reinforcement corrosion, *Cem. Concr.*
872 *Res.* 53 (2013) 59-67.
- 873 [52] D.A. Kulik, T. Wagner, S.V. Dmytrieva, G. Kosakowski, F.F. Hingerl, K.V. Chudnenko, U.R. Berner, GEM-Selektor
874 geochemical modeling package: revised algorithm and GEMS3K numerical kernel for coupled simulation codes,
875 *Computational Geosciences*. 17 (2013) 1-24.
- 876 [53] W. Hummel, U. Berner, E. Curti, F. Pearson, T. Thoenen, Nagra/PSI chemical thermodynamic data base 01/01,
877 *Radiochimica Acta*. 90 (2002) 805-813.
- 878 [54] B. Lothenbach, D.A. Kulik, T. Matschei, M. Balonis, L. Baquerizo, B. Dilnese, G.D. Miron, R.J. Myers, Cemdata18:
879 A chemical thermodynamic database for hydrated Portland cements and alkali-activated materials, *Cem. Concr. Res.* 115
880 (2019) 472-506.

- 881 [55] B.Z. Dilnesa, B. Lothenbach, G. Renaudin, A. Wichser, D. Kulik, Synthesis and characterization of hydrogarnet
- 882 $\text{Ca}_3(\text{Al}_x\text{Fe}_{1-x})_2(\text{SiO}_4)_y(\text{OH})_{4(3-y)}$, Cem. Concr. Res. 59 (2014) 96-111.
- 883 [56] C. Li, M. Wu, W. Yao, Eco-efficient Cementitious System Consisting of Belite-Ye'elite-Ferrite Cement,
- 884 Limestone Filler, and Silica Fume, ACS Sustainable Chem. Eng. 7 (2019) 7941-7950.
- 885 [57] Q. Zeng, C. Wang, Y. Luo, C. Yu, Q. Huang, C. Luo, Effect of temperatures on TSA in cement mortars under
- 886 electrical field, Constr. Build. Mater. 162 (2018) 88-95.
- 887 [58] B. Lothenbach, G. Le Saout, E. Gallucci, K. Scrivener, Influence of limestone on the hydration of Portland cements,
- 888 Cem. Concr. Res. 38 (2008) 848-860.
- 889 [59] M. Vespa, B. Lothenbach, R. Dähn, T. Huthwelker, E. Wieland, Characterisation of magnesium silicate hydrate
- 890 phases (M-S-H): A combined approach using synchrotron-based absorption-spectroscopy and ab initio calculations, Cem.
- 891 Concr. Res. 109 (2018) 175-183.
- 892 [60] O.S.B. Al-Amoudi, Attack on plain and blended cements exposed to aggressive sulfate environments, Cem. Concr.
- 893 Compos. 24 (2002) 305-316.
- 894 [61] P. Brown, S. Badger, The distributions of bound sulfates and chlorides in concrete subjected to mixed NaCl , MgSO_4 ,
- 895 Na_2SO_4 attack, Cem. Concr. Res. 30 (2000) 1535-1542.
- 896 [62] Y. Luo, C. Wang, Z. Fang, L. Xiao, Q. Zeng, The TSA degradation process of cement-based materials in the
- 897 electrical field environment, Constr. Build. Mater. 206 (2019) 703-716.
- 898 [63] R. Gollop, H. Taylor, Microstructural and microanalytical studies of sulfate attack. IV. Reactions of a slag cement
- 899 paste with sodium and magnesium sulfate solutions, Cem. Concr. Res. 26 (1996) 1013-1028.
- 900 [64] W. Kunther, B. Lothenbach, J. Skibsted, Influence of the Ca/Si ratio of the C-S-H phase on the interaction with
- 901 sulfate ions and its impact on the ettringite crystallization pressure, Cem. Concr. Res. 69 (2015) 37-49.
- 902 [65] C. Li, M. Wu, Q. Chen, Z. Jiang, Chemical and mineralogical alterations of concrete subjected to chemical attacks in

- 903 complex underground tunnel environments during 20–36 years, Cem. Concr. Compos. 86 (2018) 139–159.
- 904 [66] M. Rosenqvist, A. Bertron, K. Fridh, M. Hassanzadeh, Concrete alteration due to 55 years of exposure to river water:
- 905 Chemical and mineralogical characterisation, Cem. Concr. Res. 92 (2017) 110–120.
- 906 [67] E. Samson, J. Marchand, K.A. Snyder, J. Beaudoin, Modeling ion and fluid transport in unsaturated cement systems
- 907 in isothermal conditions, Cem. Concr. Res. 35 (2005) 141–153.
- 908 [68] E. Samson, J. Marchand, J. Beaudoin, Modeling the influence of chemical reactions on the mechanisms of ionic
- 909 transport in porous materials: an overview, Cem. Concr. Res. 30 (2000) 1895–1902.
- 910 [69] D. Conciatori, É. Grégoire, É. Samson, J. Marchand, L. Chouinard, Statistical analysis of concrete transport
- 911 properties, Mater. Struct. 47 (2013) 89–103.
- 912 [70] E. Stora, B. Bary, Q.C. He, E. Deville, P. Montarnal, Modelling and simulations of the chemo–mechanical behaviour
- 913 of leached cement-based materials: leaching process and induced loss of stiffness, Cem. Concr. Res. 39 (2009) 763–772.
- 914 [71] E. Stora, B. Bary, Q.C. He, E. Deville, P. Montarnal, Modelling and simulations of the chemo-mechanical behaviour
- 915 of leached cement-based materials: Interactions between damage and leaching, Cem. Concr. Res. 40 (2010) 1226–1236.
- 916

Table 1 Chemical and mineralogical compositions of the Portland cement (wt. %).

Chemical composition		Mineralogical composition	
Na ₂ O	0.04	C ₃ S	58.32
MgO	0.76	C ₂ S	11.64
Al ₂ O ₃	4.55	C ₃ A	3.96
SiO ₂	20.8	C ₄ AF	8.03
P ₂ O ₅	0.11	Calcite	4.58
SO ₃	2.92	Anhydrite	0.76
K ₂ O	0.74	Bassanite	3.67
CaO	64.8	Gypsum	0.01
TiO ₂	0.23	Lime	0.35
Cr ₂ O ₃	0.02	Portlandite	0.58
MnO	0.11	CF ₂	1.53
Fe ₂ O ₃	3.27	Goergeyite	3.30
CuO	0.02	Perovskite	1.79
ZnO	0.05	Periclase	0.85
SrO	0.03	Dolomite	0.13
LOI	2.58	Quartz	0.21

Table 2 Concentration of ions in the pore solution before degradation and diffusion coefficient in free water (D_i^0).

	Concentration mol/L	Diffusion coefficient 10^{-9} m ² /s	Direction
OH ⁻	2.05×10^{-1}	5.273	
SO ₄ ²⁻	6.79×10^{-4}	1.065	
AlO ₂ ⁻	4.25×10^{-5}	n.a. ¹	
SiO ₃ ²⁻	9.94×10^{-6}	n.a. ¹	Cathode → inner part → anode → anodic solution
CO ₃ ²⁻	4.66×10^{-5}	n.a. ¹	
HCO ₃ ⁻	2.27×10^{-8}	1.185	
Ca ²⁺	1.01×10^{-3}	0.792	
Ca(OH) ⁺	9.09×10^{-4}	n.a. ¹	
Mg ²⁺	1.11×10^{-10}	0.706	Anode → inner part → cathode → cathodic solution
Na ⁺	2.34×10^{-3}	1.334	
K ⁺	2.01×10^{-1}	1.957	

¹ Not available in [49].

Table 3 Mineralogical alterations of sulfate attacks induced by electric migration (this paper) and diffusion (obtained from [11,15]).

Process	Formation phase	Decomposition phase
Electric migration, cathode	Ettringite → Gypsum + Si-Al gel	Monocarbonate → Portlandite → Ettringite → C-S-H
Electric migration, anode, Na_2SO_4 ¹	Na-rich silica gel + Gypsum (surface)	Not clearly observed in the experiments
Electric migration, anode, MgSO_4 ¹	M-S-H + Brucite + Gypsum (surface)	Not clearly observed in the experiments
Diffusion, Na_2SO_4	Ettringite → Gypsum ²	Monocarbonate → Portlandite → C-S-H
Diffusion, MgSO_4	Ettringite → Brucite → Gypsum → M-S-H	Monocarbonate → Portlandite → Ettringite → C-S-H

¹ Only the experimentally verified phases are listed in the formation column. The decomposition order of the hydration products was not clearly observed in the experiments and thus is not listed in the decomposition column.

² Gypsum forms when the Na_2SO_4 concentration is high, e.g., 44 g/L in [11].

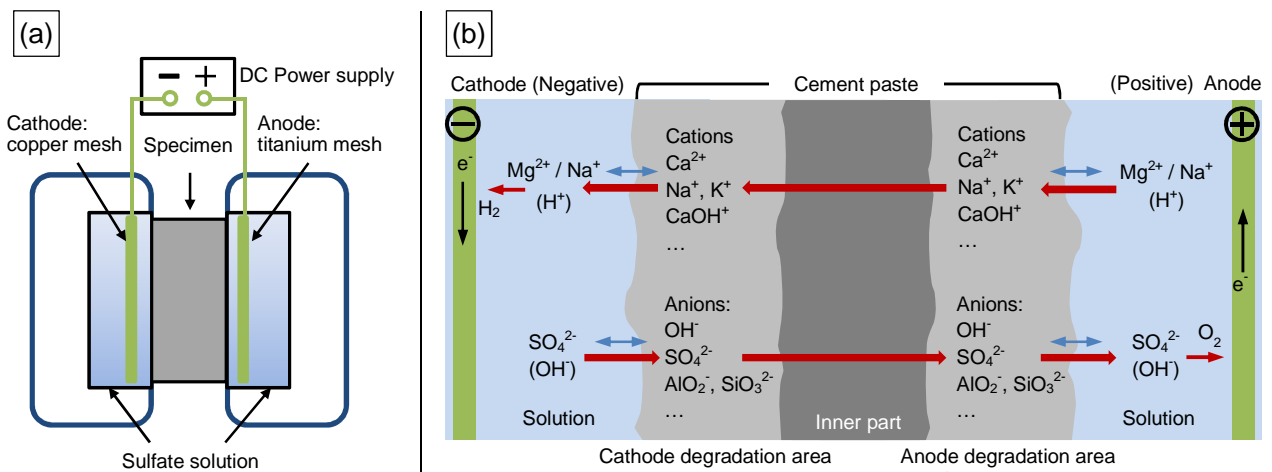


Fig. 1. Test setup to apply electric fields: (a) overview of the test setup and (b) schematic of ionic motion where thickness and velocity are not to scale. The ionic motion is driven by electric migration (red arrows) and diffusion (blue arrows).

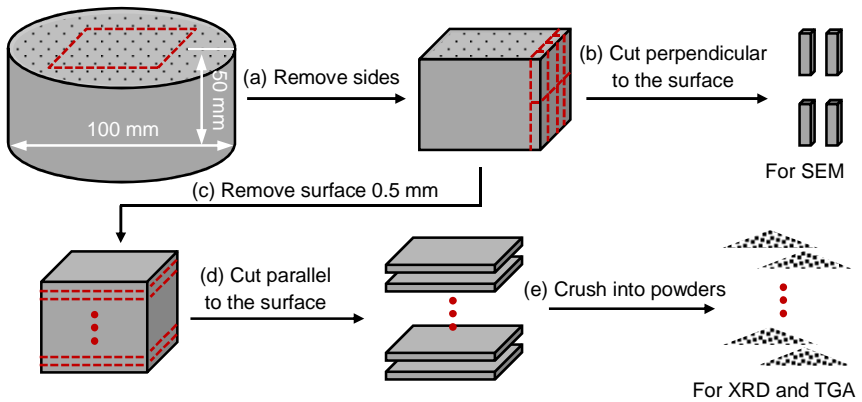


Fig. 2. Preparation of samples: (a) the sides of a cylindrical specimen that were not well exposed to sulfate solutions were cut off, (b) small patches that were perpendicular to the exposure surface was cut for SEM, (c) the surface part (0.5 mm) of the remainder was removed, (d) the specimen was cut parallel to the exposure surface into 5-mm thick slices, and (e) the slices were crushed into powders (particle size $<75 \mu\text{m}$) for XRD and TGA.

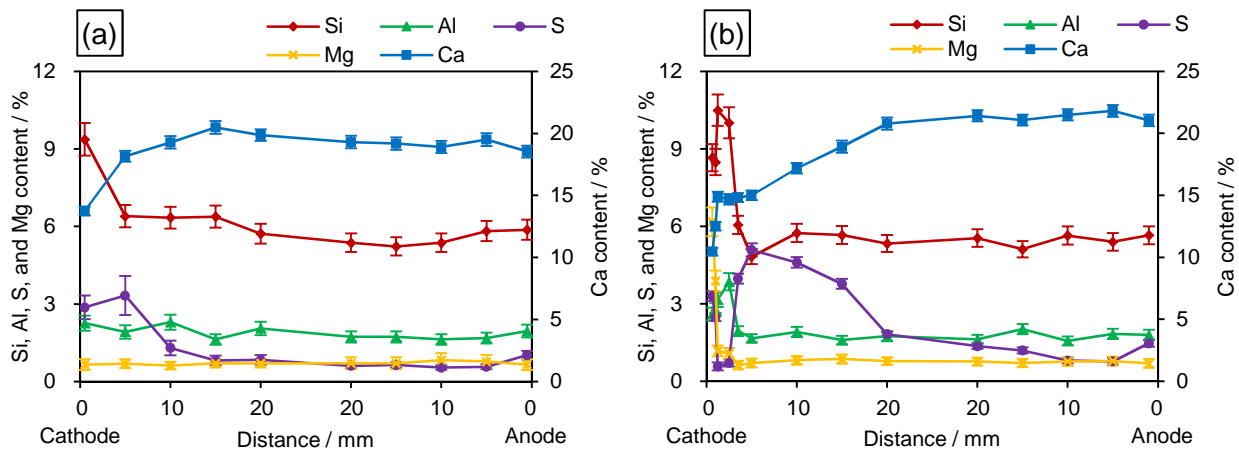


Fig. 3. Chemical composition at different distances from the surface (cathode on the left and anode on the right) after exposure to MgSO_4 for (a) 7 d and (b) 28 d. Each data point represents the average over a $50 \mu\text{m} \times 50 \mu\text{m}$ area measured by EDS. Error bars indicate the standard error in ZAF matrix correction schemes. The sampling points nearest to the surfaces are 0.1 mm from the surface.

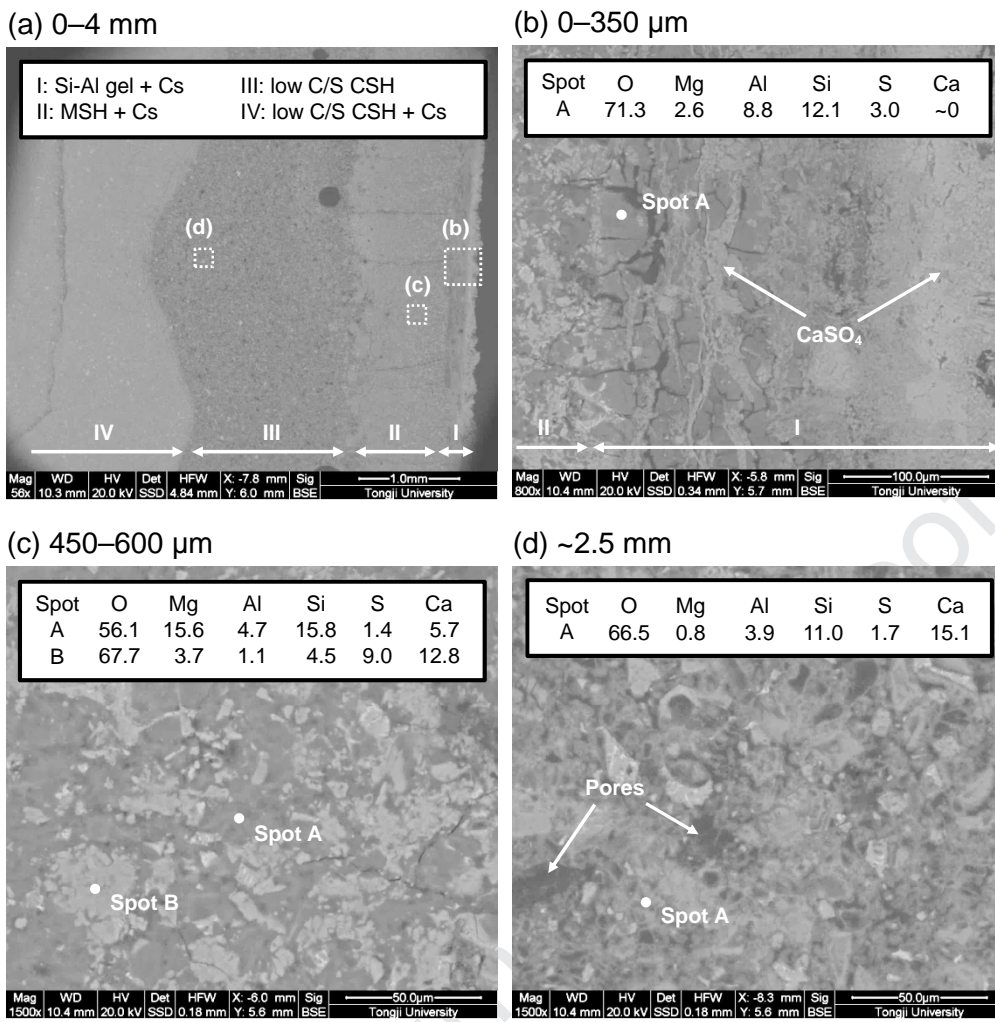


Fig. 4. Microstructure of the surface area (0–4 mm) near the cathode after 28 d exposure to MgSO₄: (a) an overview, and (b) to (d) enlargements of the squared areas. Surface on the right.

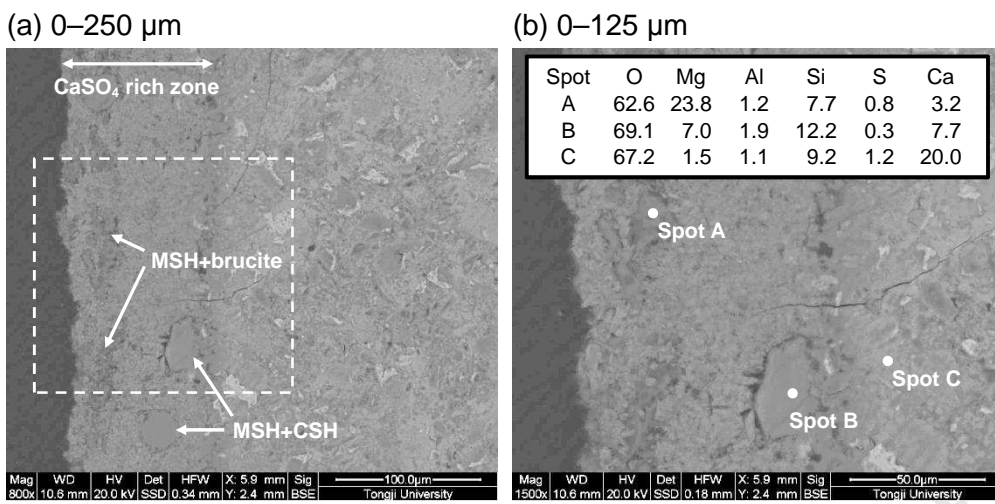


Fig. 5. Microstructure of the surface area (0–250 μm) near the anode after 28 d exposure to MgSO_4 : (a) an overview and (b) enlargement of the squared area. Surface on the left.

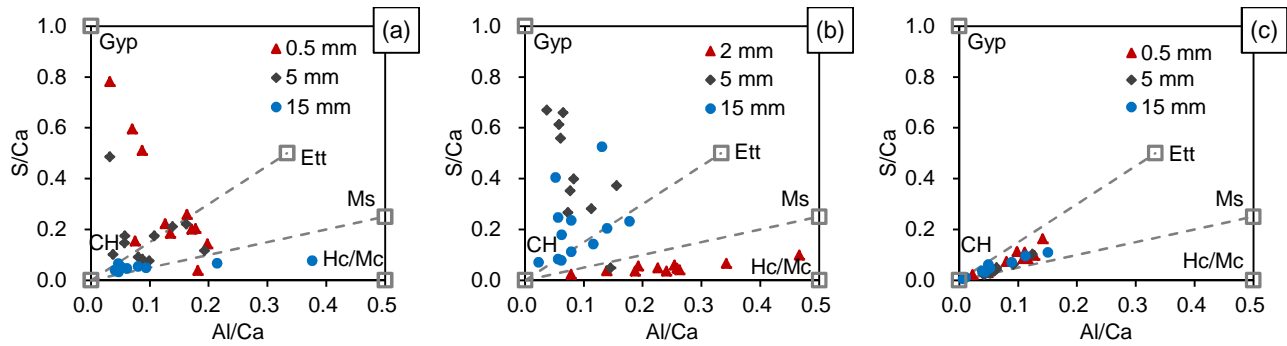


Fig. 6. Atom ratio plots of S/Ca against Al/Ca at different depths from the surface after exposures to MgSO_4 : (a) and (b) the cathode areas exposed to MgSO_4 for 7 d and 28 d, respectively; (c) the anode areas exposed to MgSO_4 for 28 d. CH = Portlandite (and C-S-H at a similar position), Ett = Ettringite, Ms = Monosulfate, Hc/Mc = Hemicarbonate or monocarbonate, Gyp = CaSO_4 .

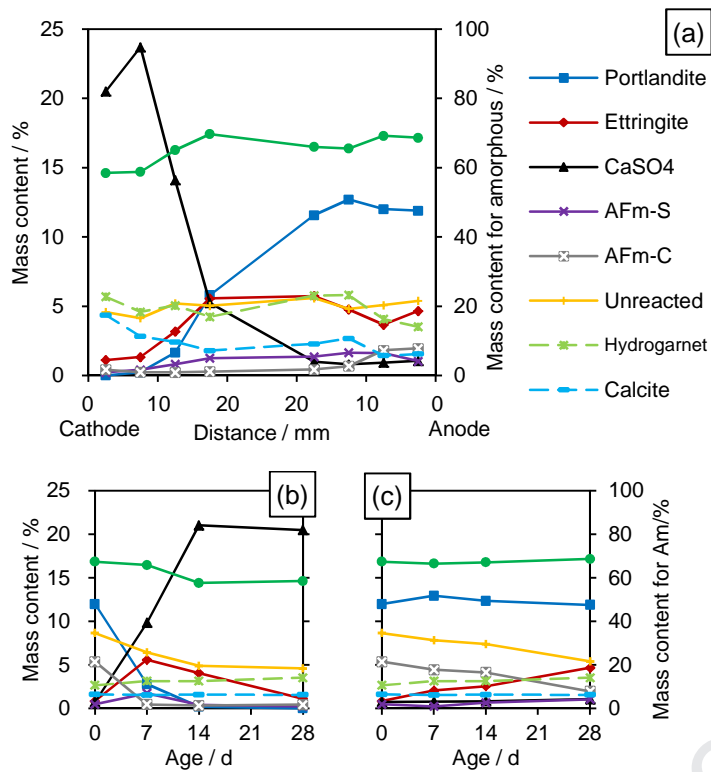


Fig. 7. Mineralogical composition of the specimen exposed to MgSO₄ obtained by XRD and Rietveld refinement: (a) all the depths after 28 d exposure time; (b) and (c) phase alteration of the 0.5–5 mm area near the cathode and anode, respectively, after different exposure time. CaSO₄ = anhydrite + bassanite + gypsum, AFm-S = monosulfate, AFm-C = monocarbonate + hemicarbonate, hydrogarnet = katoite + hydrogrossular.

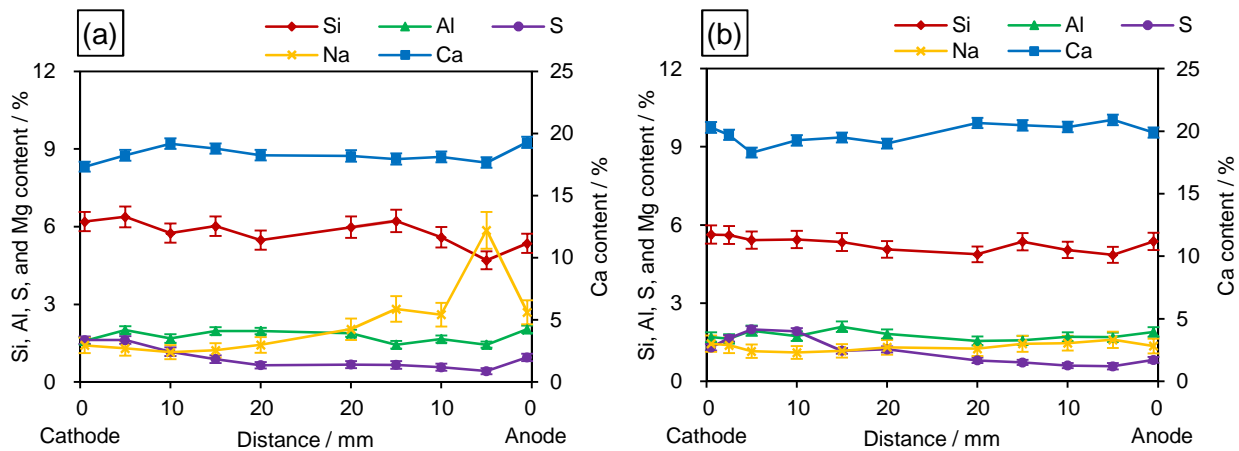


Fig. 8. Chemical composition at different distances from the surface (cathode on the left and anode on the right) after exposure to Na_2SO_4 for (a) 7 d and (b) 28 d.

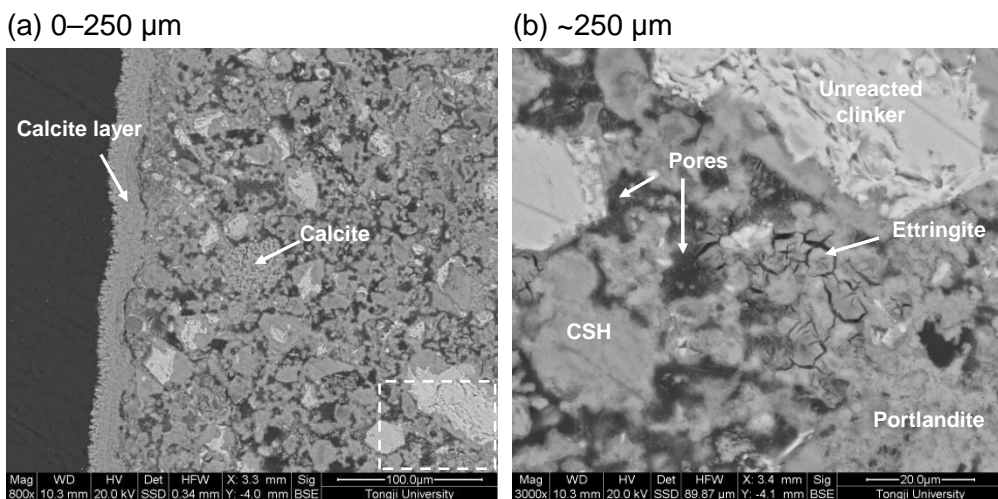


Fig. 9. Microstructure of the surface area (0–250 μm) near the cathode after 28 d exposure to Na_2SO_4 : (a) an overview and (b) enlargement of the squared area. Surface on the left.

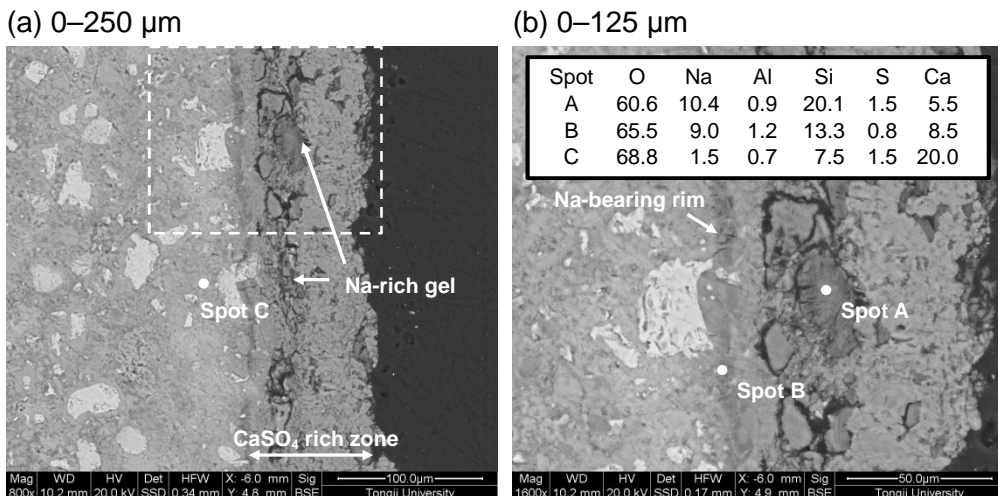


Fig. 10. Microstructure of the surface area (0–250 μm) near the anode after 28 d exposure to Na_2SO_4 : (a) an overview and (b) enlargement of the squared area. Surface on the right.

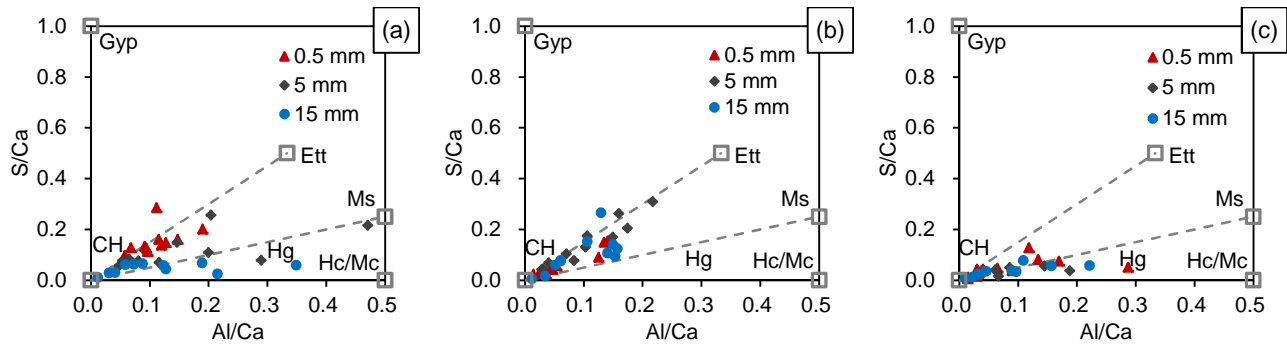


Fig. 11. Atom ratio plots of S/Ca against Al/Ca at different depths from the surface after exposures to Na₂SO₄: (a) and (b) the cathode areas exposed to Na₂SO₄ for 7 d and 28 d, respectively; (c) the anode areas exposed to Na₂SO₄ for 28 d. CH = Portlandite (and C-S-H at a similar position), Ett = Ettringite, Ms = Monosulfate, Hc/Mc = Hemicarbonate or monocarbonate, Gyp = CaSO₄.

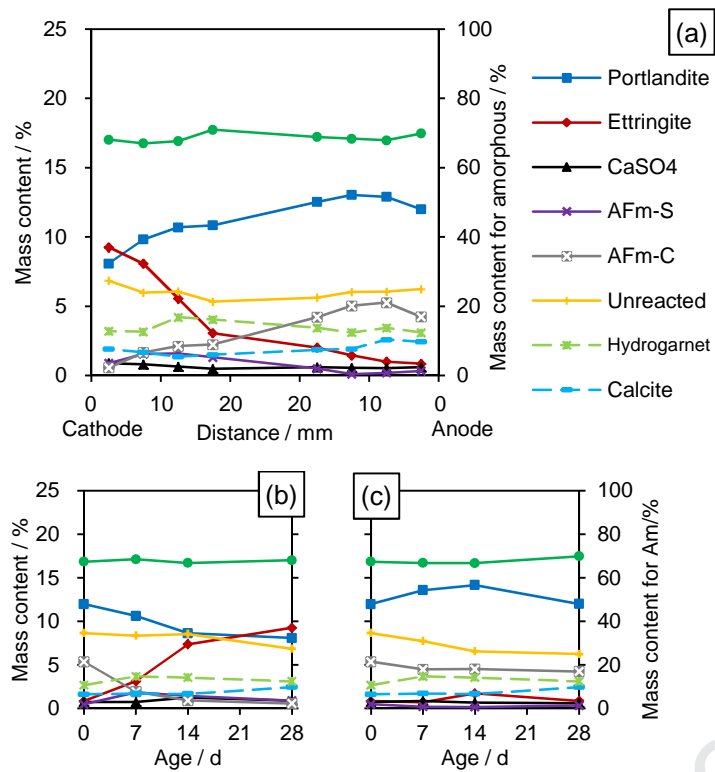


Fig. 12. Mineralogical composition of the specimen exposed to Na_2SO_4 obtained by XRD and Rietveld refinement: (a) all the depths after 28 d exposure time; (b) and (c) phase alteration of the 0.5–5 mm area near the cathode and anode, respectively, after different exposure time. CaSO_4 = anhydrite + bassanite + gypsum, AFm-S = monosulfate, AFm-C = monocarbonate + hemicarbonate, hydrogarnet = katoite + hydrogrossular.

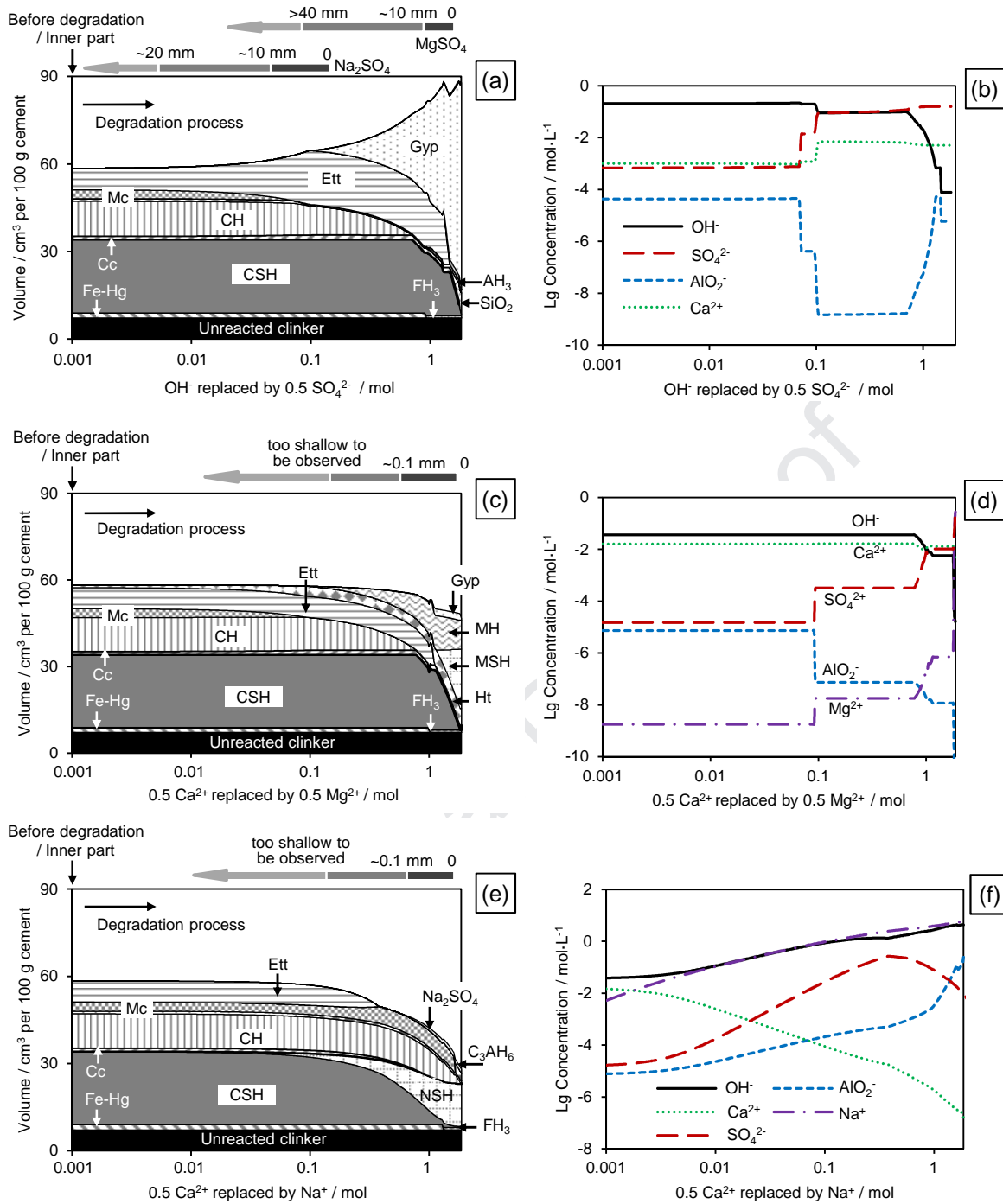


Fig. 13. Phase assemblage and pore solution chemistry during the simplified electric migration process, calculated by thermodynamic modeling: (a) and (b) the degradation process near the cathode; (c) and (d) the degradation process near the anode after MgSO₄ exposure; (e) and (f) the degradation process near the anode after Na₂SO₄ exposure. The horizontal-axis can be interpreted into the alteration in a certain position with time or the distribution of products after a certain exposure time. A logarithmic axis is used for better comparison with thermodynamic modeling studies on diffusion-induced sulfate attacks [1,2,11,14-16]. The arrows above the figures illustrate the approximate distribution of hydration products after 28 d exposure time (experimental results). CH = portlandite, Ett = ettringite, Mc = monocarbonate, Gyp = gypsum, Cc = calcite, Fe-Hg = C₃FS_{0.84}H_{4.32} and/or C₃F_{1.34}H_{3.32}, Ht = hydrotalcite, MH = brucite, MSH = M-S-H gel, and NSH = the Na end-member, [(NaOH)_{2.5}SiO₂H₂O]_{0.2} included in the CSHQ model.

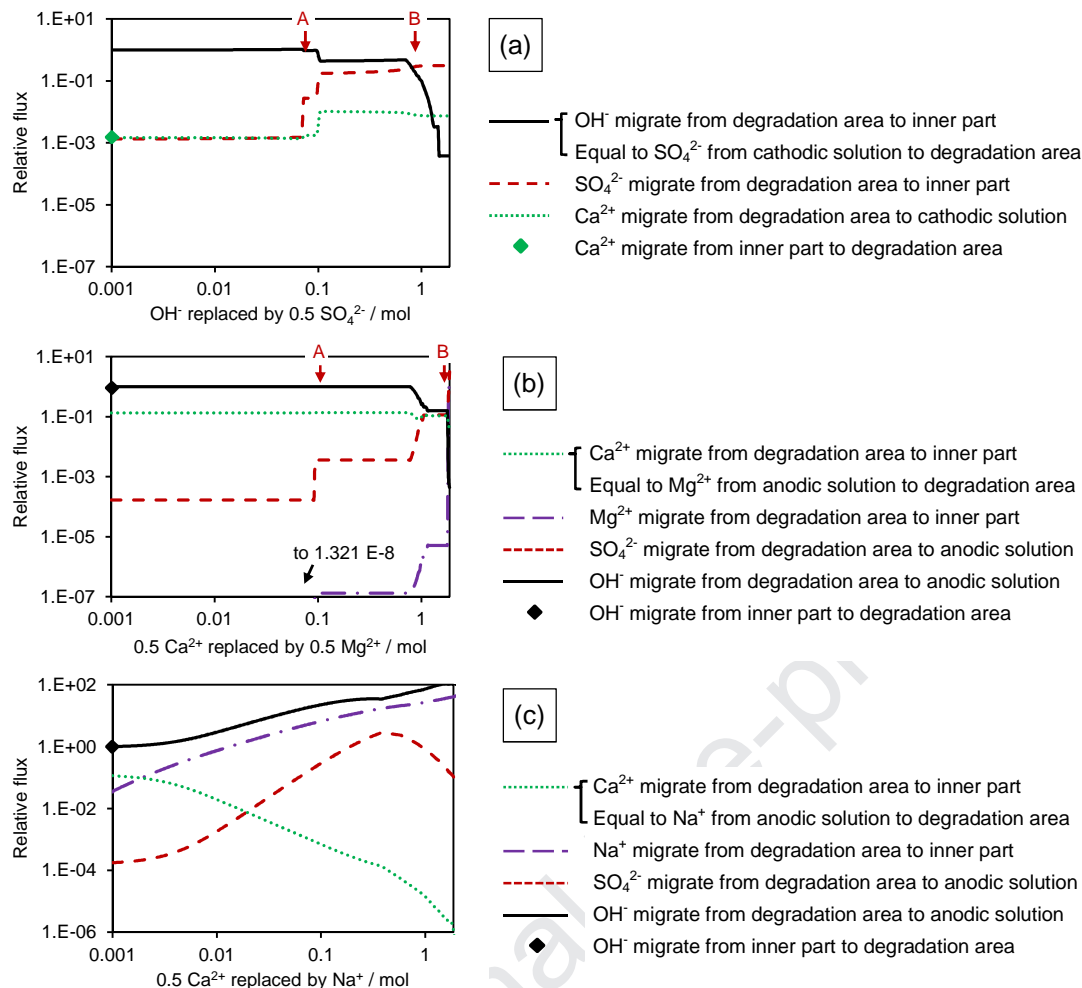


Fig. 14. The relative flux of ionic species: (a) the cathode area; (b) and (c) the anode area exposed to MgSO_4 and Na_2SO_4 , respectively. The cations and anions migrate in different directions, see Fig. 1b. Certain ionic species are compensated by those from the inner part of the specimen, and the compensation rate is marked by a diamond (provided that the ionic strength in the inner part of the specimen remains stable). The square bracket indicates the ionic species in the external solution is transported into the degradation area with the same relative flux to certain ions based on the assumption of charge balance.

Conflict of interest

None.